universität wien

MASTERARBEIT / MASTER'S THESIS

Titel der Masterarbeit / Title of the Master's Thesis

Upgrade of ASACUSA's Antihydrogen Detector

verfasst von / submitted by

Viktoria Kraxberger, BSc

angestrebter akademischer Grad / in partial fulfilment of the requirements for the degree of

Master of Science (MSc)

Wien, 2022 / Vienna, 2022

Studienkennzahl lt. Studienblatt / degree programme code as it appears on the student record sheet:	A 066 876
Studienrichtung lt. Studienblatt / degree programme as it appears on the student record sheet:	Master Physik / Master's degree programme Physics
Betreut von / Supervisor:	Dr. Johann Zmeskal, Privatdoz.

Kurzfassung

Das ASACUSA (Atomic Spectroscopy And Collisions Using Slow Antiprotons) Experiment am Antiproton Decelerator von CERN hat das Ziel die Hyperfeinaufspaltung im Grundzustand von Antiwasserstoff und Wasserstoff zu vergleichen und bietet damit einen direkten Test der CPT-Symmetrie.

Das ASACUSA-Hodoskop detektiert sekundäre Teilchen (hauptsächlich Pionen), die bei der Annihilation des Antiprotons von Antiwasserstoff produziert werden. Es ist ein fassförmiger, achteckiger Detektor bestehend aus einer äußeren und inneren Lage von jeweils 32 Plastikszintillator-Balken und zwei Lagen szintillierenden Fasern. Jeder Balken wird an beiden Enden mit Silicon Photomultipliers (SiPMs) ausgelesen, jede Faser (100 in der äußeren, 64 in der inneren Lage) mit einem SiPM. Diese SiPMs sind an IFES boards (Intelligent Frontend Electronics for SiPMs) angeschlossen, welche zuvor am Stefan-Meyer-Institut entwickelt wurden und neben einer Vorverstärkung auch ein digitales Time-over-Threshold (ToT) Signal mittels Leading-Edge-Diskriminierung erzeugen.

Zuvor war die mögliche Detektionsrate des Hodoskops in etwa 50 Hz. Um diese zu erhöhen war es nötig mehrere Änderungen im Datenaufnahme-System vorzunehmen. Neben einer Überarbeitung des Datentransfers der Time-to-Digital Converters (TDCs), wurden auch Teile der Datenaufnahme-Software neu programmiert. Diese Änderungen ermöglichten eine Datenaufnahme mit einer Rate von über 1000 Hz.

Die ToT-Signale des Hodoskops werden in eine FPGA-Logik geleitet um ein Trigger-Signal aus Koinzidenzen zu produzieren, sie werden aber auch genutzt um Zeitmessungen mit den TDCs durchzuführen.

Durch die Leading-Edge-Diskriminierung der ToT mit einer fixen Schwelle variiert die Leading Edge mit der Höhe des analogen Signals. Um einen Weg zu finden, diesen „Time Walk“ zu umgehen, wurden mehrere Testmessungen durchgeführt.

Abstract

The ASACUSA (Atomic Spectroscopy And Collisions Using Slow Antiprotons) experiment located at the Antiproton Decelerator at CERN aims to compare the ground state hyperfine splitting of antihydrogen to hydrogen, providing a direct test of the CPT symmetry.

The ASACUSA hodoscope detects the secondary particles produced by annihilation of the antiproton of antihydrogen, which are mostly pions. It is a barrel-type octagonal detector consisting of an outer and an inner layer of 32 plastic scintillator bars each and two layers of scintillating fibres. The bars are individually read out by two silicon photomultipliers (SiPMs) on each end of the bar and additionally every fibre (100 in the outer layer, 64 in the inner) is read out by a SiPM. The SiPMs are connected to IFES boards (Intelligent Frontend Electronics for SiPMs), previously developed at the Stefan-Meyer-Institute, which are pre-amplifiers and provide a digital time-over-threshold (ToT) signal via leading edge discrimination.

Previously, the possible detection rate of the hodoscope was at about 50 Hz. In order to provide detection at a higher rate, several changes had to be made in the data acquisition (DAQ) system.

After performing changes in the data transfer of the time-to-digital converters (TDCs) as well as reprogramming the DAQ software, events at a rate of over 1000 Hz could be detected without loss.

The ToT signals of the hodoscope bars are fed into FPGA logic units to produce a trigger from coincidences but are also used for further time measurements with TDC units.

Since the ToT signals are produced by leading edge discrimination with a fixed threshold, the position of the leading edge varies with the height of the corresponding analogue signal produced. To find a way to prevent this time-walk effect, several test measurements were performed.

Acknowledgements

First and foremost I want to thank Hannes for supervising me through this thesis and his constant support. Thank you for sharing not only your expertise and knowledge, but especially your enthusiasm for experimental particle physics and lab work.

My gratitude also goes to Eberhard for providing the opportunity to work at the SMI and in the ASACUSA collaboration and offering your guidance.

A big thank you goes to Svetlana who was my partner throughout this project. Thank you for your support, sharing your knowledge and also keeping up with my frustrations along the way.

A special thanks needs to go to Kaku, who not only helped us out with his skills but also always took the time to answer all my questions. Without you this thesis would have taken much longer.

Thank you to Martin and Dan for taking the time and reading through this thesis.

Working at the SMI would not be the same without the colleagues.
Marlene and Vici, both of you provided the best possible start into this master's thesis. Thank you for all of your advice along the way and of course all the fun we had together in the lab and in the office.
I would like to thank Doris, Gerhard and Mark for their support and even though the pandemic rarely made social gatherings possible, I want to thank Amit, Alina, Carina, Marcus and Waleed for the fun game nights and the Heurigen excursion.

Apart from the people at the institute I want to thank Stefan for doing the first proof-read of this thesis, even though you said it was as easy to read as a user manual written in Chinese. Thank you for always being there for me. Thank you for everything.

Contents

1 Introduction

The Standard Model builds the foundation of modern particle physics. It describes the elementary particles and the fundamental forces (except for gravity), but it fails to explain some still unresolved issues like the abundance of matter compared to antimatter in our universe. Due to this, particle physics is looking for physics beyond the Standard Model.

1.1 Symmetries

A symmetry in physics means that a system remains the same after a transformation – it is invariant. With Noether's theorem it was proven that symmetries lead to conservation laws [1].
The discrete CPT symmetries, individually described in the following, build the fundamentals of the Standard Model of particle physics:

- Parity transformation P is an inversion of the space parameter $\mathbf{r} \rightarrow -\mathbf{r}$ and therefore reverses helicity
- Charge conjugation C changes the sign of all charges, meaning it transforms a particle p into its antiparticle $\bar{p}$
- Time reversal T inverts the time $t \rightarrow -t$

The invariance of these symmetries was not questioned until P was proven to be broken in weak interactions by Wu in the 1950s [2]. After that, also C and CP invariance were found to be broken [3].
Until today, only the invariance under the combination of all three transformations, CPT, could not be disproved. Together with Lorentz invariance this builds the basis of quantum field theory [4].
When performing such a CPT transformation on a wave function $\psi(t, \mathbf{r})$, the involved particle is converted into an antiparticle in a mirrored universe:

$$\mathsf{CPT}\ \psi(t, \mathbf{r}) \rightarrow \psi^*(-t, -\mathbf{r}) \tag{1.1}$$

To fulfill this, the properties of matter and antimatter must be the same, except for changing the sign of charges and magnetic momenta. For this reason precision measurements of these quantities provide a good test of the CPT theorem.

1.2 Baryon Asymmetry

As a conclusion of the Standard Model, antimatter and matter should behave symmetrically and in the Big Bang theory matter and antimatter are thought to be produced equally. The over-abundance of matter in the universe we observe today suggests there must be some asymmetry that explains this phenomenon.
In 1967 Sakharov proposed three criteria that need to be met in order to explain the existing baryon asymmetry [5]:

- Baryon number violation
  There must exist a process in which the baryon number is not conserved and more matter is produced than antimatter. This must have happened at one specific time where soon after, the process becomes unlikely again.
- Interactions out of thermal equilibrium
  If there was thermal equilibrium in the early universe, the process producing more baryons than antibaryons would also happen in reverse, resulting in again the same amount of matter and antimatter. So the universe must have been in some temporary out-of-equilibrium stage.
- C and CP violation
  If these symmetries were intact, baryon and antibaryon producing processes would happen at the same rate, again resulting in no baryon asymmetry.

As stated in section 1.1, C and CP violation has already been proven, but only in very little amounts that do not suffice to explain the baryon asymmetry. This is where CPT violation would come in. The theoretical framework of the Standard Model Extension, described in section 2.2, includes CPT violating terms that can produce a larger baryon asymmetry [6].

2 Theoretical Background

This section gives an overview of the theoretical basics used in the $\overline{\mathrm{H}}$ Hyperfine Spectroscopy by the Atomic Spectroscopy And Collisions Using Slow Antiprotons (ASACUSA) collaboration described in chapter 3 and is needed for the experimental work described in this thesis.

2.1 Hyperfine structure

The ASACUSA collaboration aims to measure the hyperfine structure of antihydrogen to compare its value to that of hydrogen.
The sum of the total angular momenta of the electron (or positron) $\boldsymbol{J}$ and the proton (or antiproton) $\boldsymbol{I}$ defines the total angular momentum $\boldsymbol{F}$ of the (anti)hydrogen atom. The quantum number F must follow $|I - J| \leq F \leq |I + J|$ and the magnetic quantum number m_F can take any integer value between $-F$ and F.
Due to this, the ground state of (anti)hydrogen splits up into a singlet state for $F = 0$, $m_F = 0$ and a triplet state for $F = 1$, $m_F = (-1, 0, 1)$. For a hydrogen atom in the state (F, m_F) the corresponding antihydrogen state changes the sign of the magnetic quantum number to (F, $-m_F$).
The transition frequency between the $F = 0$ and $F = 1$ states at vanishing external magnetic field is the so-called hyperfine transition frequency or hyperfine splitting frequency ν_{HFS}, which has been determined in various experiments. The most precise measurement has been done in maser experiments resulting in [7, 8]:

$$\nu_{\mathrm{HFS}} = (1\,420\,405\,751.7667 \pm 0.0009)\,\mathrm{Hz} \tag{2.1}$$

The hyperfine splitting frequency has also been measured with beam spectroscopy by the ASACUSA group, yielding in a relative precision of 2.7×10^{-9} [9] superseding the previous measurement from the 1950s that resulted in a relative precision of 5×10^{-8} [10]. Contrary to in-beam experiments, measuring the hyperfine splitting of antihydrogen with a maser can currently not be realised since the (anti-) atoms need to be in a matter confinement.
The hyperfine structure Hamiltonian is defined as

$$\mathcal{H} = Ag\hat{\boldsymbol{I}}\hat{\boldsymbol{J}} + \hat{\boldsymbol{\mu}}\boldsymbol{B} \tag{2.2}$$

with the zero field hyperfine splitting constant A, the Landé factor g, total angular momentum operators of the nucleus and the electron $\hat{\boldsymbol{I}}$ and $\hat{\boldsymbol{J}}$, the operator of the

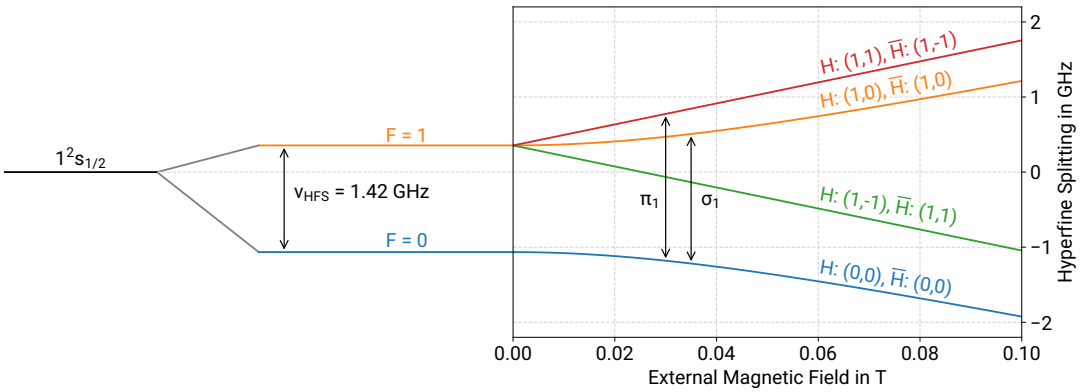

Fig. 2.1.: Ground-state hyperfine splitting without and with external magnetic field of hydrogen and antihydrogen. The arrow on the left indicates the transition frequency ν_{HFS} between the hyperfine states with $F = 0$ and $F = 1$. In the Breit-Rabi diagram the states of (F, m_F) are labelled for both H and $\overline{\mathrm{H}}$ and the arrows indicate two of the possible transitions.

magnetic moment of the nucleus $\hat{\boldsymbol{\mu}}$ and the external magnetic field $\boldsymbol{B}$.
If no external field is present, the energy splitting is just $\Delta E = Ag = h\nu_{\mathrm{HFS}}$, which is the case we have discussed before. Under the influence of an external magnetic field B, the degenerate triplet state splits into three seperate components. The energy of the splitted states is also described by the Breit-Rabi formula [11, 12]

$$E_{I\pm\frac{1}{2},m_F} = -\frac{\Delta E}{2(2I+1)} \pm \frac{\Delta E}{2}\sqrt{1+\frac{4m_F}{(2I+1)}\cdot\chi+\chi^2} \tag{2.3}$$
$$\chi = \frac{g_J\mu_B B}{\Delta E}$$

using the Landé factor of the electron g_J and the Bohr magneton μ_B. For (anti)hydrogen in ground state the nuclear angular momentum I is $\frac{1}{2}$. In Fig. 2.1 on the left side the ground state hyperfine splitting is depicted and on the right side the Breit-Rabi diagram shows the further splitting with a present external magnetic field for the various states of hydrogen or antihydrogen.

To calculate the magnetic moment of (anti)hydrogen one takes the derivative of the Breit-Rabi formula with respect to the total magnetic field [11, 12].

$$-\frac{\partial E_{I\pm\frac{1}{2},m_F}}{\partial|\boldsymbol{B}|} = \mu_{m_F} = \mp\frac{\frac{2m_F}{2I+1}+\chi}{\sqrt{1+\frac{4m_F}{2I+1}\cdot\chi+\chi^2}}\mu_B \tag{2.4}$$

For an inhomogenous external magnetic field the four states can be divided into low field seeking and high field seeking as seen in Fig. 2.2. This means that atoms in a low field seeking (LFS) state experience a force towards lower field regions while atoms in high field seeking (HFS) states do the opposite.

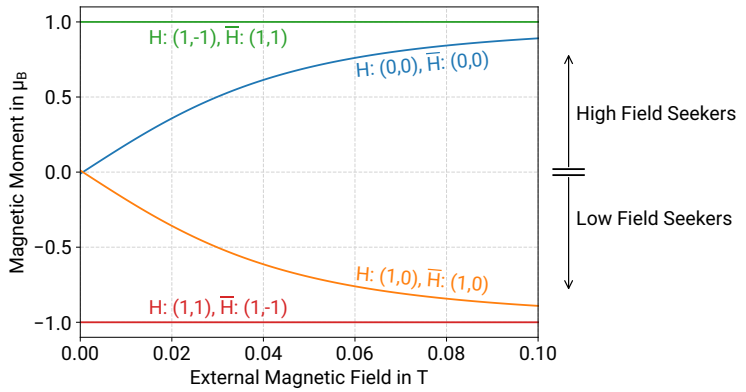

Fig. 2.2.: While forming three groups in the low-field regime, in sufficiently strong inhomogenous external magnetic fields the ground-state hyperfine states can be categorised into two groups by looking at their magnetic moments. LFS states drift towards lower magnetic field strengths and HFS states move towards higher magnetic field strengths.

2.2 Standard Model Extension

The Standard Model Extension (SME) forms a theoretical framework developed by Alan Kostelecký and colleagues that introduces spontaneous breaking of CPT and Lorentz invariance (LI). In the Standard Model Extension the Dirac equation is modified to include CPT violating and Lorentz invariance violating terms [13]:

$$\left(i\gamma^\mu D_\mu - m_e \underbrace{- a^e_\mu \gamma^\mu - b^e_\mu \gamma_5 \gamma^\mu}_{\text{violate CPT and LI}} \underbrace{- \frac{1}{2} H^e_{\mu\nu} \sigma^{\mu\nu} + i c^e_{\mu\nu} \gamma^\mu D^\nu + i d^e_{\mu\nu} \gamma_5 \gamma^\mu D^\nu}_{\text{only violate LI}}\right) \psi = 0 \quad (2.5)$$

in natural units $c = \hbar = 1$ with the derivative $D_\mu = \partial_\mu + iqA_\mu$, the electron mass m_e, γ^μ are the Dirac matrices[1] where $\gamma_5 = i\gamma_0\gamma_1\gamma_2\gamma_3$ and a Dirac spinor ψ. The charge $q = -|e|$, $A^\mu = (|e|/4\pi r, 0)$ is the proton Coulomb potential and a^e_μ, b^e_μ, $H^e_{\mu\nu}$, $c^e_{\mu\nu}$ and $d^e_{\mu\nu}$ are SME coefficients.

For hydrogen and antihydrogen this would mean energy-shifts in the hyperfine levels depending on some of the SME constants, whose sizes are expected to be small but need to be determined through experiments [14].

To arrive at the SME-Hamiltonian of hydrogen $\mathcal{H}^{\text{SME}}_{\text{H}}$, a leading order perturbation $\delta\mathcal{H}_{\text{H}}$ is added to the Dirac Hamiltonian $\mathcal{H}_{\text{H}}$. The energy shifts can then be determined by calculating the matrix elements of this $\delta\mathcal{H}_{\text{H}}$ [15]:

$$\langle nFJLm'_F|\delta\mathcal{H}_{\text{H}}|nFJLm_F\rangle = \sum_{jm} A_{jm}\langle Fm_F jm|Fm'_F\rangle \quad (2.6)$$

[1] $\gamma_0 = \begin{pmatrix} \mathbb{1}_{2\times2} & 0 \\ 0 & -\mathbb{1}_{2\times2} \end{pmatrix}, \gamma_i = \begin{pmatrix} 0 & \sigma_i \\ -\sigma_i & 0 \end{pmatrix}$ for $i = 1, 2, 3$

$\sigma_1 = \begin{pmatrix} 0 & 1 \\ 1 & 0 \end{pmatrix}$, $\sigma_2 = \begin{pmatrix} 0 & -i \\ i & 0 \end{pmatrix}$, $\sigma 3 = \begin{pmatrix} 1 & 0 \\ 0 & -1 \end{pmatrix}$ are the Pauli matrices.

The unperturbed state $|nFJLm_F\rangle$ is an eigenstate with principal quantum number n, total angular momentum F, electron angular momentum quantum number J, orbital angular momentum number L and magnetic quantum number m_F. The weights $A_{jm}(nFJL)$ encapsulate the relevant SME coefficients, here m is the angular momentum projection. For the relevant cases in ground-state hyperfine splitting of $F = 0$ and $F = 1$ the energy shifts $\delta\epsilon$ can be determined as [15]:

$$F = 0 : \qquad \delta\epsilon(n, L) = A_{00} \tag{2.7}$$

$$F = 1 : \quad \delta\epsilon\left(n, L, \frac{1}{2}, m_F\right) = A_{00} + \frac{1}{\sqrt{2}} m_F |\boldsymbol{A}| \qquad |\boldsymbol{A}| \equiv \sqrt{\sum_m A_{1m}^* A_{1m}} \tag{2.8}$$

The weight $A_{00}(nL)$ cannot be measured through transition frequencies with $\Delta n \neq 0$ or $\Delta L \neq 0$, but the vector $\boldsymbol{A}$ is formed by anisotropic SME coefficients and can be imagined as a background field which lifts the degeneracy in the $F = 1$ states [15, 16]. A possible example of that can be seen in Fig. 2.3, where the shifts of hydrogen and antihydrogen were assumed to be opposite, but neither the sign nor the magnitude of these shifts are really known.

In addition of being a model-independent CPT test, measuring the hyperfine transition frequencies of hydrogen and antihydrogen would therefore provide a test of the theoretical framework of the Standard Model Extension.

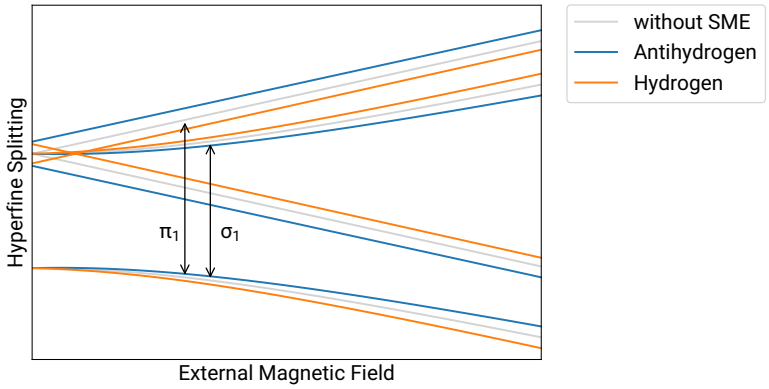

Fig. 2.3.: Example for a SME ground-state hyperfine splitting with external magnetic field of hydrogen (orange) and antihydrogen (blue). The lifted degeneracy in the $F = 1$ state (also at no external magentic field) can be seen. The magnitudes and signs of the shifts are not predicted by the SME. In grey you can see the Breit-Rabi diagram without Standard Model Extension, as seen before in Fig. 2.1.

2.3 Annihilation

When antimatter and matter particles interact, they annihilate. While electrons and positrons as leptons emit photons of their combined energies, composite particles like baryons can produce other particles in the annihilation process.
The antiproton is made up of 3 antiquarks ($\bar{u}, \bar{u}, \bar{d}$) and bound together by gluons as well as additional quark-antiquark pairs. When interacting with matter, these antiquarks will annihilate with the proton and neutron quarks and form mesons.
In the annihilation of an antiproton with a proton or neutron mostly pions are produced, see Tab. 2.1. At ASACUSA the tracking of these pions in addition to the detection of the energy deposition at the annihilation site can result in high $\overline{H}$ detection efficiency and background reduction.

Tab. 2.1.: Annihilation products from antiprotons and protons or neutrons. Data from [17], table adapted from [16].

Branching ratios (%) for $\bar{p}+p$			Branching ratios (%) for $\bar{p}+n$		
$2\pi^+ + 2\pi^- + n\pi^0$	$n \in [0, ..., 3]$	47.30	$2\pi^+ + 2\pi^- + n\pi^0$	$n \in [0, 1]$	59.7
$\pi^+ + \pi^- + n\pi^0$	$n \in [0, ..., 4]$	41.53	$2\pi^+ + 3\pi^- + n\pi^0$	$n \geq 0$	27.6
$3\pi^+ + 3\pi^- + 2\pi^0$	$n \geq 0$	4.25	$\pi^- + n\pi^0$	$n \geq 0$	16.4
$K^\pm + K^0 + \pi^\mp + \pi^0$		0.47	$3\pi^+ + 4\pi^- + n\pi^0$	$n \geq 0$	0.39
$K^\pm + K^0 + \pi^\mp$		0.46			
$K^+ + K^- + nK^0$	$n \in [0, 1]$	0.34			
$K^+ + K^- + \pi^0$		0.24			
$K^+ + K^-$		0.10			

2.4 Detector types

The ASACUSA antihydrogen detector is built out of different kinds of materials, which will be described in the following.

2.4.1 Scintillators

The energy lost along a particle's way is denoted as stopping power $-\frac{dE}{dx}$. In a scintillator this energy is converted into visible light.

Plastic Scintillators

Some of the most common scintillating materials are organics, like plastic scintillators made of polymeres. They offer an extremely fast signal and high light output. Another advantage is their flexibility as they can be produced in many shapes and sizes [18].
The energy of the particle is absorbed and an electron is excited, now populating one of the vibrational levels in the S_1 band, see Fig. 2.4.
The decay from the vibrational levels to the S_1 base state happens without radiation,

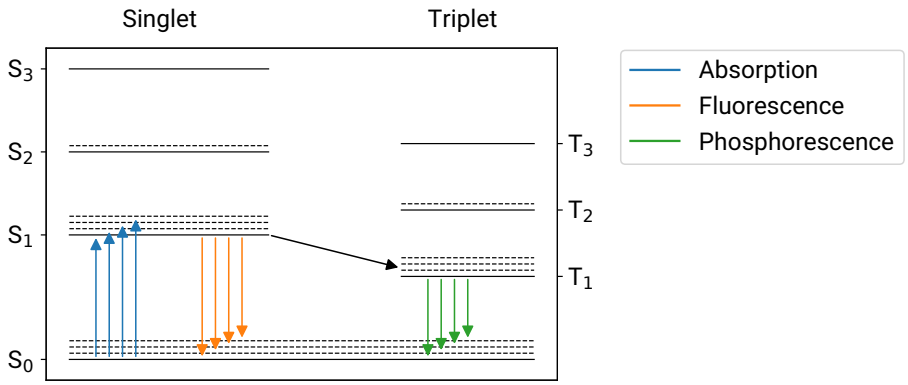

Fig. 2.4.: Energy levels of organic scintillator molecules. The solid lines show the base states, while the dashed lines are the vibrational levels of the bands. Once an electron is excited in a higher energy level there are two different ways of de-excitation – one over the triplet T_1 state (phosphorescence) and one directly back into the S_0 state (fluorescence).

while light is emitted when decaying back to the S_0 band, this direct decay is called fluorescence.
It is also possible that it first decays to the triplet T_1 state, whose energy is lower than the singlet S_1 state. De-excitation from T_1 to S_0 takes longer and the light emitted is called phosphorescence. Since these two processes have different decay times the number of emitted photons $N(t)$ can be described through

$$N(t) = A \exp\left(-\frac{t}{\tau_f}\right) + B \exp\left(-\frac{t}{\tau_s}\right) \tag{2.9}$$

with A, B weight factors and the fast and slow decay times τ_f, τ_s [18].
Polyvinyltoluene scintillators like EJ-200 which is used in ASACUSA's antihydrogen detector (see section 4.2) have a maximum wavelength emission of 425 nm, a rise time of 0.9 ns and a decay time of 2.1 ns . The scintillation efficiency is 10 000 photons per 1 MeV electron [19].

Inorganic Crystal Scintillators

Inorganic crystals like $Bi_4Ge_3O_{12}$ (BGO) have a high density and a high atomic number. Therefore they offer a high stopping power. This is also the reason for using it as a central calorimeter in the ASACUSA detector, see section 4.1.
The density of the BGO crystal is 7.13 g/cm^3. The maximum scintillation emission wavelength is at 480 nm and the decay time is 300 ns at room temperature [20].

2.4.2 Silicon Photo Multipliers

In order to convert the emitted photons of the scintillator into an electrical signal, a photo detector is needed. One type is the silicon photo multiplier (SiPM) which is an array of several thousand micro avalanche photodiodes (APDs), all operated in Geiger mode [21]. Due to the operation above breakdown voltage V_{BD}, a dark current range of a few µA can be measured, which is caused by thermal electrons. In Figure 2.5 the current density is plotted against the relative overvoltage and the typical operation range of a SiPM is indicated.
For the antihydrogen detector KETEK PM3350 SiPMs were used which have a maximum photo detection efficiency of about 38 % at 430 nm [22].

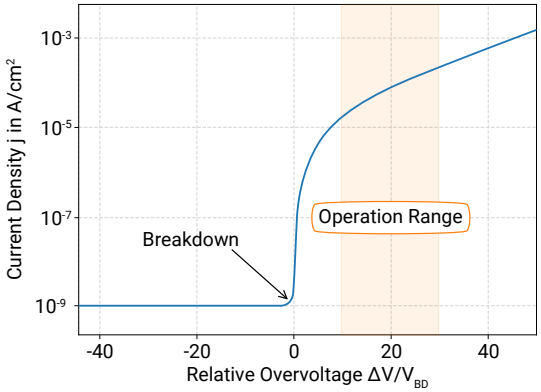

Fig. 2.5.: Example of current density against relative overvoltage in a SiPM. In orange the typical operation range is marked.

3 The ASACUSA Antihydrogen Beam Experiment

The Atomic Spectroscopy And Collisions Using Slow Antiprotons (ASACUSA) CUSP experiment is located at the Antiproton Decelerator (AD) at CERN. Its goal is to measure the difference of the hyperfine splitting in hydrogen and antihydrogen and thereby testing the CPT theorem.
Antihydrogen can only be produced with a present antiproton beam. At the end of 2018 the so-called Long Shutdown 2 (LS2) started at CERN meaning there was no beam until summer 2021.

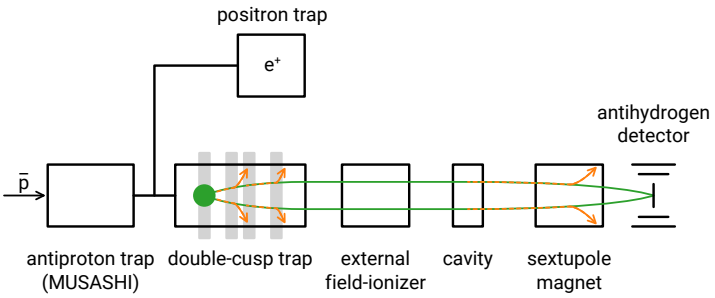

Fig. 3.1.: Scheme of the ASACUSA experiment: Inside the double-cusp trap the antiprotons from MUSASHI and positrons are combined to form antihydrogen, where only the low field seeking atoms (green) escape the trap while the high field seekers (orange) annihilate on the walls. The external field ionizer allows determination of the principle quantum number n before the atoms pass on to the cavity where a spin flip is induced. In the final sextupole magnet only the low field seekers are focused onto the detector where the annihilation products are measured.

Fig. 3.1 shows the scheme of the experiment indicating the tracks of high field seeking (orange) antihydrogen atoms and low field seeking (green) $\overline{\mathrm{H}}$ atoms. In this chapter the operating principles of the components will be discussed.

3.1 Antiproton Source

In order to form antihydrogen atoms, a source of slow antiprotons is needed.
Accelerated protons with energies of 26 GeV coming from the proton synchrotron (PS) are shot into a thin Iridium rod [23] and antiprotons are produced through the process of [24]

$$p_{\mathrm{beam}} + p_{\mathrm{target}} \rightarrow p + p + p + \overline{p} \tag{3.1}$$

The resulting antiprotons with momenta of 3.57 GeV/c are too energetic for trapping and spectroscopy experiments, therefore they need to be cooled down in the AD synchrotron and the newly built ELENA (Extra Low Energy Antiprotons) ring, see Fig. 3.2 [25].

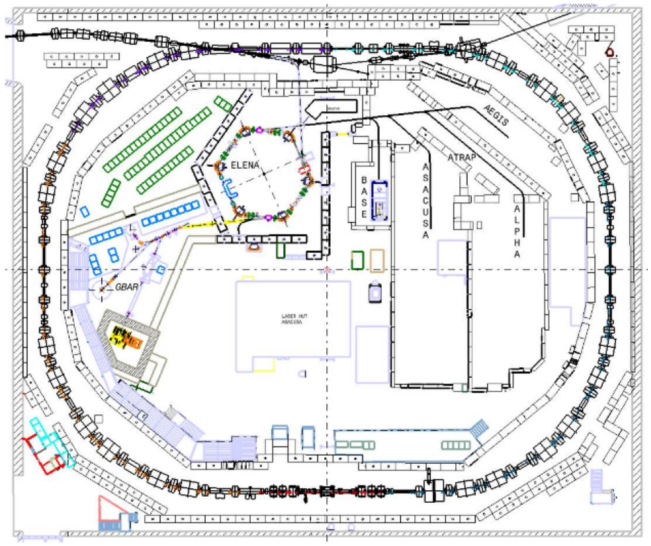

Fig. 3.2.: ELENA inside of the AD hall, the experiments inside of the AD ring are also indicated [25].

3.1.1 Deceleration

The antiprotons with a momentum spread around 3.57 GeV/c are injected into the AD and get decelerated in three steps with different cooling processes which are needed due to rising beam emittance. After the first two deceleration steps stochastic cooling is used. Electron cooling is applied after the last step until the particles have a momentum of 100 MeV/c and a kinetic energy of 5.3 MeV, see Fig. 3.3 [24].

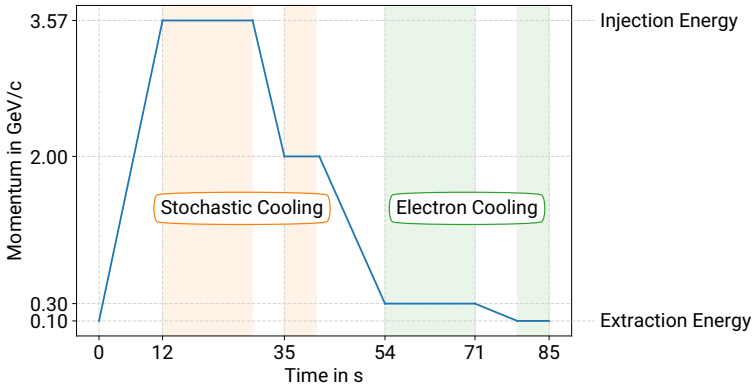

Fig. 3.3.: Cooling process in the AD, the antiprotons are injected at 3.57 GeV/c and extracted at 0.1 GeV/c. After the first two deceleration steps down to a momentum of 0.3 GeV/c stochastic cooling is and after the third one electron cooling is used [24]. The time scale can vary due to longer pauses in between the processes.

To slow down the antiprotons even further, a new synchrotron ring was built in the AD hall - the Extra Low Energy Antiprotons (ELENA) Ring, see Fig. 3.2, which is able to decelerate antiprotons to kinetic energes of 100 keV. After deceleration to an intermediate plateau of about 650 keV, as well as at the final extraction at energies of 100 keV electron cooling is applied [26].

3.1.2 Trapping

After the deceleration, the antiprotons are injected into the Monoenergetic Ultra-Slow Antiproton Source for High-precision Investigation (MUSASHI) trap, a Penning-Malmberg-type catching trap which confines the particles by a static electromagnetic field provided by multi-ring electrodes (MREs). It is possible to extract antiprotons at kinetic energies of 150 eV or 250 eV from this trap [27].

3.2 Positron Source

To get positrons, a ^{22}Na source is used, which decays over β^+ and thereby produces positrons of about 0.2 MeV. These are first slowed down with a solid neon moderator and then transferred to a nitrogen buffer gas trap [28] where they thermalise through inelastic collisons. The positrons are accumulated for $\approx$ 30 sec and are guided into the mixing trap by a magnetic field.

3.3 Antihydrogen Production

In order to form antihydrogen the antiprotons and positrons need to be combined, which is done in the double-CUSP trap [29]. This trap consists of multi-ring electrodes (MREs) and two sets of anti-Helmholtz coils forming two positions where there is zero magnetic field and high magnetic field gradients. In the mixing region the electric potential builds a nested well in which the positrons are loaded and confined, see the orange line in Fig. 3.4 on the left. After slow antiproton injection from MUSASHI, the potential is opened as indicated by the dashed line in the figure and antihydrogen is formed. The $\overline{\mathrm{H}}$ atoms are neutral and can escape the trap.
After the mixing region of the potential there is a steep potential well with strong electrostatic field, the field ionization (FI) well. Some of the atoms are in highly excited states ($n \geq 40$) and when passing this well, they are ionized and their $\overline{\mathrm{p}}$ remain inside the field ionization (FI) well [30].
Depending on their state, the remaining antihydrogen atoms are either focused or defocused by the inhomogenous double-cusp field, whose magnetic field lines are indicated in Fig. 3.4 on the right. The defocused atoms are high field seekers and annihilate on the walls, while the others then form a low field seeking polarised beam [30].

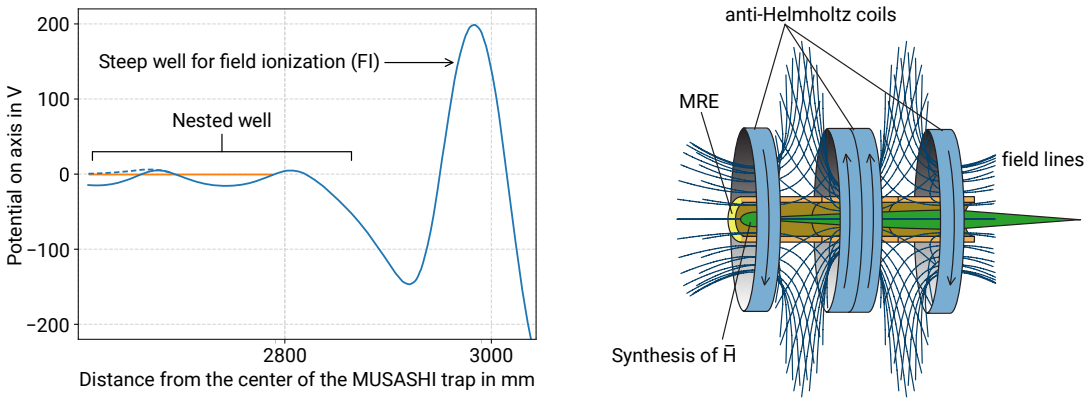

Fig. 3.4.: Left: Potential inside the double-CUSP trap with the nested well forming the mixing region and the steep well for field ionization. The solid line is before $\overline{\mathrm{p}}$ injection and the dashed line during $\overline{\mathrm{p}}$ injection. The orange line shows the maximal potential of the confined positrons in the well [30]. Right: Double-CUSP trap consisting of two sets of anti-Helmholtz coils and MREs [16].

To detect the annihilations on the wall and distinguish them from annihilations in the residual gas in the trap, the ASACUSA Micromegas Tracker (AMT) [31] was built around the MRE at the mixing region of the CUSP. The AMT has a half-cylindrical form and uses two layers of Micro-MEsh GAseous Structure (Micromegas) and one layer of scintillators between them. The scintillators are used for triggering the Micromegas readout.

3.3.1 Mixing Scheme

In the previous beam times the preferred mixing scheme has been "direct injection" where about 3×10^5 antiprotons from MUSASHI were injected into the positron plasma in the nested well (see Fig. 3.4, left) [32]. The dominant processes in ASACUSA's antihydrogen production is three-body recombination [33]:

$$\overline{\mathrm{p}} + \mathrm{e}^+ + \mathrm{e}^+ \rightarrow \overline{\mathrm{H}}^* + \mathrm{e}^+ \tag{3.2}$$

The number of antihydrogen atoms in ground state depends on the the positron temperature and density.
During the time of the LS2 at CERN some upgrades to the CUSP trap were performed. The plasma temperature will be reduced from around 200 K to under 25 K. This results in the number of ground state atoms increasing by a factor of 100 [33]. The $\overline{\mathrm{H}}$ production rate of 2 % [34] is expected to increase to $30 - 40$ % with the now cooled plasma. The mixing cycle will only take about one second compared to the previous cycle of about 100 s. Up to 1000 antihydrogen atoms per second should reach the hodoscope – this is the reason why a higher readout speed is needed.

3.4 Spectroscopy Beamline

After the double CUSP trap, an external field ionizer (EFI) chamber is used to evaluate the principal quantum number n of the antihydrogen atoms leaving the trap. It is made of two parallel copper mesh-electrodes perpendicular to the beam direction and creates a strong (tunable) electrostatic field. By applying voltages of $\pm 5\,\mathrm{kV}$ resulting in an electric field $|\boldsymbol{E}| \approx 10\,\mathrm{kV\,cm^{-1}}$, only atoms with $n < 14$ are able to pass [16].
To perform Rabi spectroscopy a spin flip needs to be induced in the beamline. This is done by the microwave cavity placed after the EFI. The cavity is surrounded by two pairs of coils which are responsible for a small, homogeneous magnetic field $\boldsymbol{B}_{\mathrm{hom}}$. The microwave cavity produces an oscillating magnetic field $\boldsymbol{B}_{\mathrm{osc}}$ with a frequency corresponding to the hyperfine transition frequency ν_{HFS} of 1.42 GHz which induces the spin flips. The detuning range of the cavity is 12 MHz allowing to reach the resonance frequencies of the σ_1 and π_1 transitions.
The orientation of $\boldsymbol{B}_{\mathrm{hom}}$ in respect to $\boldsymbol{B}_{\mathrm{osc}}$ decides whether the σ_1 or π_1 transition can be measured. The fields need to be parallel to measure the σ_1 transition ($(1,0) \rightarrow (0,0)$) and perpendicular for the π_1 transition ($(1,-1) \rightarrow (0,0)$), see Fig. 2.1 before [16].
Focussing the low field seeking atoms onto the detector as well es defocussing the high field seekers is done by a superconducting sextupole magnet after the cavity with a pole strength of 3.5 T [16].
The detector at the end of the beamline measures the annihilation products of the $\overline{\mathrm{H}}$ and thereby acts as a counter of annihilation events. In the following chapter the detector and its working principle will be discussed in more detail since this is the main focus of this thesis.

4 The ASACUSA Antihydrogen Detector

The ASACUSA antihydrogen detector is a barrel-type detector consisting of an outer and an inner layer of 32 plastic scintillator bars each and two layers of scintillating fibres, see Fig. 4.1. The bars are individually read out by two silicon photomultipliers on each end of the bar and additionally every fibre (100 in the outer layer, 64 in the inner) is read out by a SiPM. In the center a crystal scintillator is placed as a calorimeter.

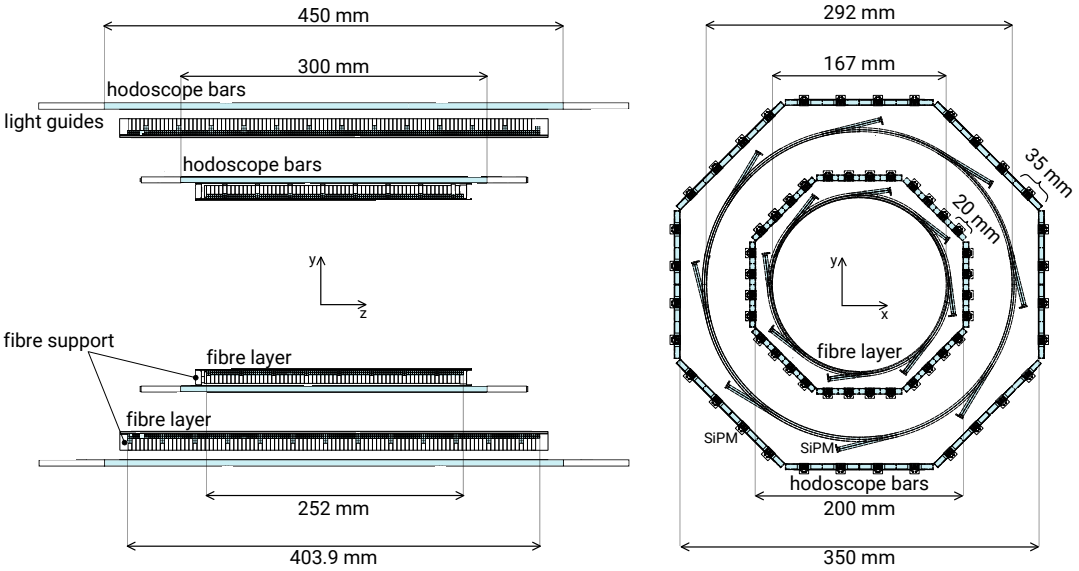

Fig. 4.1.: Cross sections of the hodoscope in the y-z plane (left) and x-y plane (right). In the left the hodoscope bars with lightguides as well as the fibre layers including their support are shown and on the right also the SiPM positions are shown. The dimensions of the parts are indicated [16].

4.1 Central Calorimeter

In the center of the detector there is the end of the beamline vacuum chamber, a CF-100 beam pipe. In it a BGO crystal scintillator disc of 90 mm diameter and 5 mm thickness is placed in front of a vacuum window. Between this and the disc there is a small gap. On the outside of the window four Hamamatsu H8500 multi-anode photo multiplier tubes (PMTs) with an area of $49\times49\,\mathrm{mm}^2$ with each 8×8 pixels are connected with optical grease.

The antiproton of the incoming antihydrogen annihilates on the surface of the BGO. The annihilation products (see table 2.1) travel through the scintillator and photons

are produced that travel through the vacuum window to the PMTs. The signals go through Clear Pulse CP80190 amplifier units, directly attached to the photo multiplier tube. They perform charge-amplification, digitise and read out the signals that are then sent to a ClearPulse CP80057 Versa Module Europa (VME) bus card. This allows the readout of the particle position with a 16×16 pixel resolution (one pixel is $\approx 6 \times 6\,\mathrm{mm}^2$) and its energy deposit [35].

4.2 Bar Hodoscope

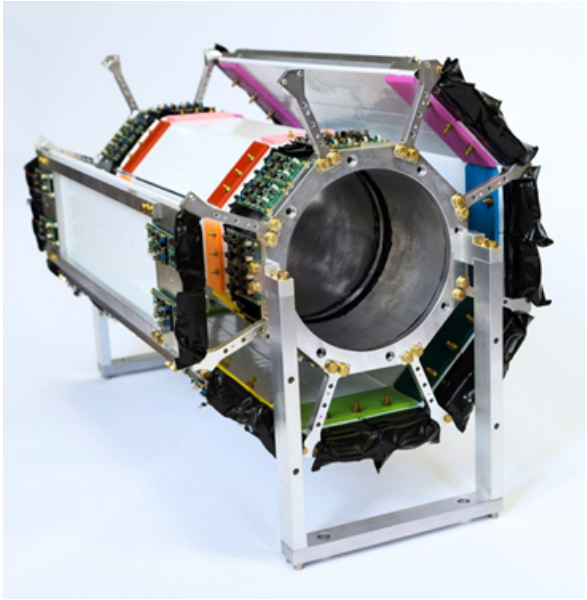

Fig. 4.2.: Hodoscope detector with two layers of 32 scintillator bars read out on each end. This picture still shows the before used amplifier boards mounted directly on the bars. Two upper segments were dismounted for better visuals [36].

The bar hodoscope (Fig. 4.2) is a barrel-type detector in octagonal shape. It is made up of two layers of 32 scintillating bars each. The bars are Eljen Technology EJ-200 plastic scintillators. The outer bars are 450 mm long, 35 mm wide and 5 mm thick, the inner bars are $300 \times 20 \times 5\,\mathrm{mm}^3$. Trapezoidal light guides are glued onto each side of the bar, so the surface at the end is only $8 \times 5\,\mathrm{mm}^2$. The smaller surface matches the two silicon photo multipliers (SiPMs), that are connected in series and glued with optical cement onto each end of the bars. KETEK 3350-TS SiPMs with $3 \times 3\,\mathrm{mm}^2$ active area were used.
In the course of B. Kolbinger's PhD thesis each bar of the hodoscope was wrapped in aluminium foil and covered in light-tight foil to optimize the signals [16].
The SiPMs are connected to pre-amplifier boards, called intelligend frontend electronics for SiPMs (IFES) and previously developed at the Stefan-Meyer-Institute by C. Sauerzopf and H. Schneider [37, 38]. Each has 16 input channels and amplified analogue outputs as well as digital time-over-threshold (ToT) outputs via leading edge discrimination. The board houses Arduino micro-controllers which allow to set the

gain of the analogue signals as well as the threshold for the ToT signals through a USB connection. The signals are produced as low voltage differential signals (LVDSs), transferred via long twisted pair flat band cables. The differential signal is used to cancel noise that is picked up.
Overall there are 128 hodoscope channels which can be divided in 4 subgroups - outer downstream, outer upstream, inner downstream and inner upstream.
An annihilation event produces particles in the center of the hodoscope and then travel first through the inner layer and then through the outer. In a similar manner comic rays produce signals in the hodoscope while transversing. Since they come from the outside they travel first through one outer layer, then through the inners and again through one outer layer. Cosmic particles are travelling nearly at the speed of light, covering 300 mm in about 1 ns. The diameter of the hodoscope is 350 mm. By measuring the time-of-flight (ToF) it is therefore possible to distinguish real events and cosmic events, provided the time resolution for the difference of two bars' mean times Δm is < 1 ns. For particles produced in the center Δm should be ≈ 0.
Until the last beam time at CERN in 2018, the analogue signals were connected to five CAEN V1742 waveform digitiser module. Due to this, a readout at rates higher than about 50 Hz was not possible. The digital signals were transferred to a CAEN V1495 field programmable gate array (FPGA) logic modules and used to produce a trigger signal.
In 2021 the whole hodoscope was shipped to Vienna. In the course of this thesis the event trigger mechanism was then simplified and the digital signals are now also transferred to CAEN V1190 time-to-digital converters (TDCs). The details of these upgrades are the subject of this thesis and will be described in the following chapters.

4.3 Fibre Detector

In 2017 an upgrade to the hodoscope detector was made by M. Fleck [39]. Two layers of scintillating fibres were added to the detector – one between the bar layers and one on the inside, see Fig. 4.1 for the exact placements.
Since the bar hodoscope only provides good position resolution in the x-y plane, this system was added to also have position resolution in z-direction. The outer layer consists of 100 scintillating fibre bundles, the inner layer is made up of 64. Each Saint Gobain BCF-12 fibre is wound around one time and four of the $2 \times 2\,\mathrm{mm}^2$ fibres form one bundle. They are arranged as a 2×2 matrix to be read out together by a KETEK PM3350-EB SiPM on one end. The same frontend electronics are used as for the hodoscope bars and only the digital ToT signals are readout by two CAEN V1190 (A and B) TDCs [40, 41].

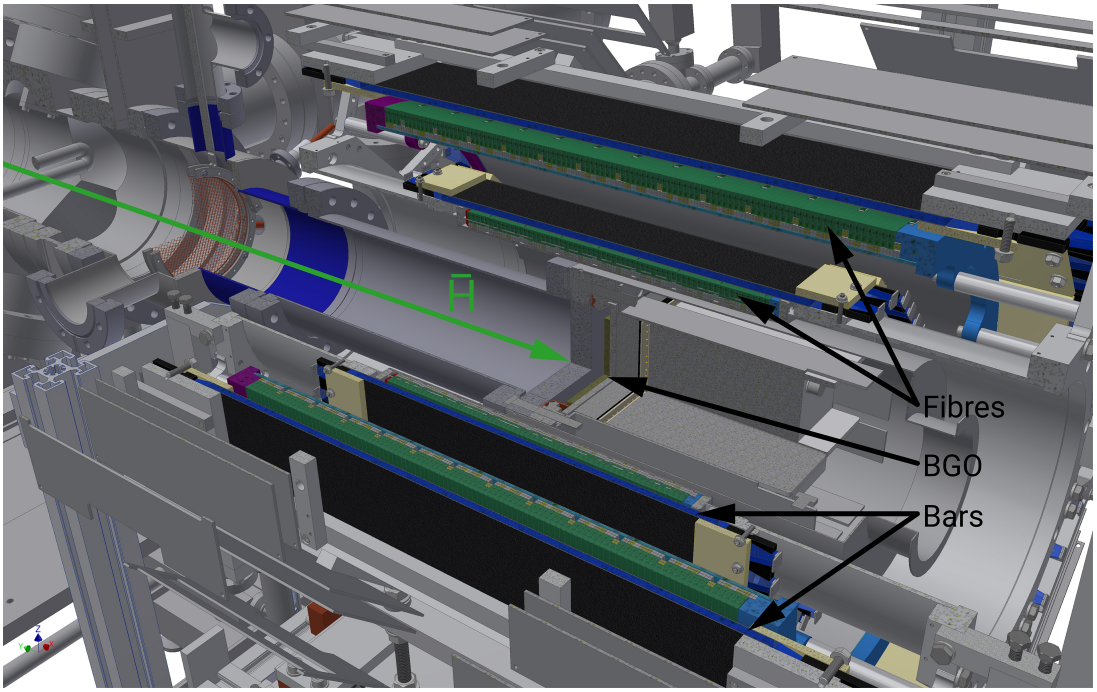

Fig. 4.3.: The antihydrogen detector inside the beamline. The green arrow shows the direction of the incoming $\overline{H}$. The BGO, fibres and bars are also marked. Technical drawing done by D. Pristauz-Telsnigg.

4.4 Data Acquisition

In total three TDCs are used – for the hodoscope bars one CAEN V1190A and for the fibres a V1190A and V1190B. They are housed inside a W-IE-NE-R VME crate together with a SIS3104 VME sequencer, a "PCI express to VME interface". The SIS is connected to a PC via optical link to transfer the taken data to the Maximum Integrated Data Acquisition System (MIDAS). For each event the data is then stored into a MIDAS file which is then transformed into a ROOT[1] file by the `analyser` , a programme written to pre-analyse the raw binary data.
Improvements to the data acquisition (DAQ) system together with the `analyser` programme will be further discussed in chapter 6.

[1]ROOT is a data analysis framework developped by CERN [42, 43]

5 Event Trigger Upgrade

A trigger signal is used to start measuring only under certain conditions and to avoid taking unnecessary amounts of data. The previously used trigger mechanism was changed in 2021 as described in the following.

5.1 NIM-Module Trigger System

Until the last beam time in 2018 a trigger system using several nuclear instrumentation standard (NIM) logic modules was applied together with an FPGA VME unit. The ToT signals of the hodoscope bars were transferred into the FPGA (CAEN V1495 "General Purpose VME Board"). A coincidence signal was produced when there was a signal for both the upstream and downstream SiPM of at least one outer bar and one inner bar, the scheme is shown in Fig. 5.1.

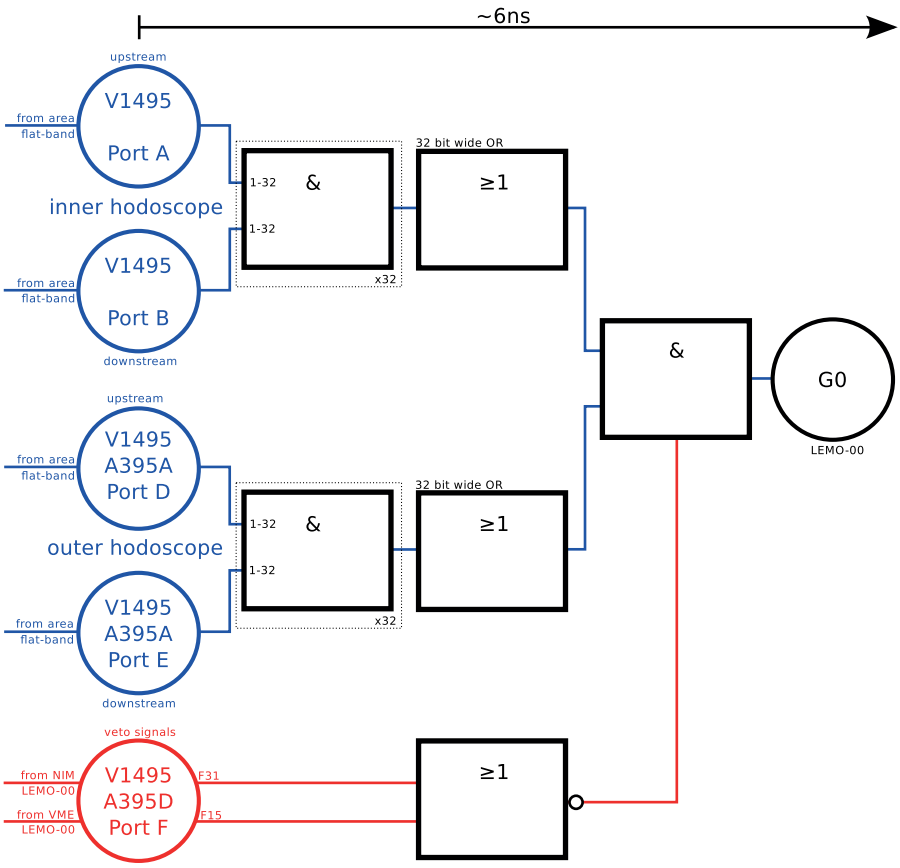

Fig. 5.1.: FPGA logic created by C. Sauerzopf [37]. Veto signals are red, the small circle symbolises signal inversion. The output of the V1495 is called G0.

This coincidence signal was then further processed using a gate generator and a coincidence unit was used to produce the final trigger when signals from the FPGA and the BGO are present. The whole trigger flow is shown in Fig. B.1.
The AD veto is needed due to the high amount of noise during AD injection. The Brescia trigger comes from large scintillating bars located $\approx 1\,\mathrm{m}$ downstream from the CUSP trap ("downstream scintillator"). The BGO dynode trigger is an output on the PMTs providing a trigger if there is a signal in at least one channel.

Tab. 5.1.: Trigger types in the old setup, x means we do not care [37].

Trigger Name	Inner Hodoscope	Outer Hodoscope	BGO	Downstream Scintillator
MIP Trigger	0	0	1	1
Hodoscope only	≥ 1	≥ 1	x	x
BGO only	x	x	1	x
Event Trigger	≥ 1	≥ 1	1	x

As seen in Tab. 5.1 there were four different kinds of triggers, but only two of them were used in the setup:

- MIP/Calibration Trigger
  This trigger is active when there are annihilations on the beampipe walls or inside the CUSP trap if charged pions produce signals in the BGO and the downstream scintillator.
- Event Trigger
  This is the "real event trigger" which is active when there is a signal on at least one inner and one outer bar as well as the BGO dynode trigger. It was produced using a NIM coincidence unit, which can be seen in Fig. B.1.

After the LS2 at CERN the usage of a NIM crate should be avoided. In the next section the updated trigger scheme using only VME modules is described.

5.2 Upgrade to FPGA Trigger System

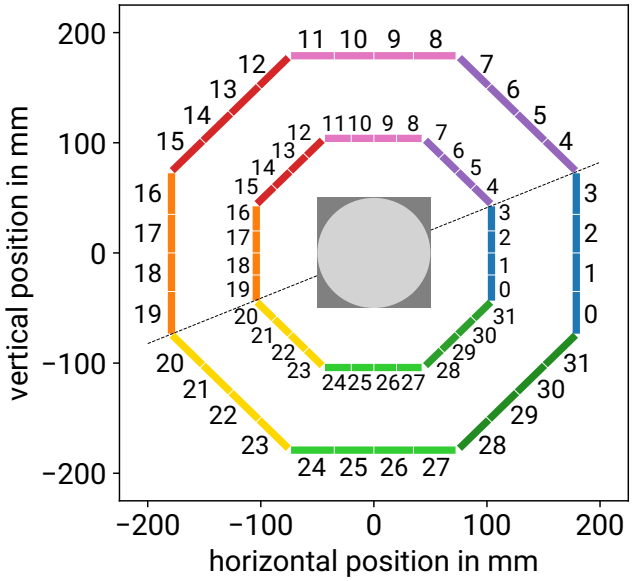

Fig. 5.2.: Cross section of the hodoscope bars in the x-y plane, the numbering of the outer and inner bars is shown. The signals of the bars above the dashed line are transferred to FPGA0, while the signals of the bars below the line are transferred to FPGA1. In the center the BGO scintillator is indicated (light gray) together with the PMTs (dark gray).

For the new setup two FPGA units (CAEN V2495 "Programmable Logic Units PLUS" [44]) were used. Each one has 6 ports, two of them are used as 32-channel LVDS inputs, two as 32-channel LVDS outputs. Since the hodoscope has 128 channels the readout had to be split up into the two logic units. In Fig. 5.2 a cross section of the hodoscope is drawn together with a dashed line showing the splitting of the readout. All channels above the line are fed into FPGA0, while all of the channels below the line are transferred to FPGA1. Since there are 16 channels on one IFES board, 8 outer channels and 8 inner channels are connected to one board. In Tab. 5.2 the distribution of bars to the boards and FPGA units is shown.

The logic was programmed using SCICompiler [45], a "User Firmware Generator and Compiler for CAEN Programmable Boards" automatically generating VHDL (Very High Speed Integrated Circuit Hardware Description Language) code from logic block diagrams. Inside the FPGA logic coincidences between the upstream and downstream ends of a bar are made to avoid triggering on dark noise of a single SiPM. If there is at least one signal on one outer bar and one inner bar, a logic impulse is produced inside the FPGA unit. Since only half of the bars are connected to one unit, this coincidence signal of FPGA1 is transferred to FPGA0 via a LEMO 00 connection. Inside FPGA0 they are linked with an or-condition to create the final coincidence trigger.

The trigger has a self-veto to avoid events being too close to each other and interfering with the transfer process. This is done by a 1 ms gate produced right after the coincidence signal. Additionally a veto signal is sent from the SIS 3104 VME to VME

Tab. 5.2.: 8 inner and 8 outer channels with the same numbers are connected to one IFES board. The upper half of the bars are connected to the FPGA unit 0 and the lower half to the FPGA unit 1. The positions of the bars can also be seen in Fig. 5.2.

	Bar	IFES Board	FPGA Unit
Downstream	4-11	A0	0
	12-19	A1	0
	20-27	B0	1
	28-31, 0-3	B1	1
Upstream	4-11	D1	0
	12-19	D0	0
	20-27	E0	1
	28-31, 0-3	E1	1

link for the duration of the readout and during antiproton injection a veto signal is sent from the AD. The final vetoed trigger signal is distributed to the 3 TDC units and the SIS 3104 module. The whole trigger logic can be seen in Fig. 5.3.

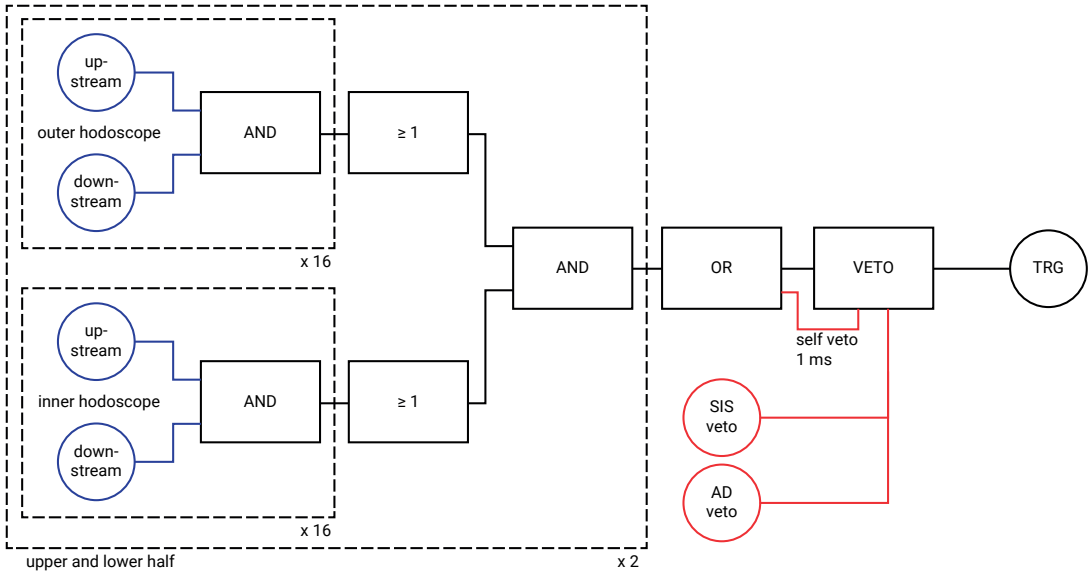

Fig. 5.3.: Upgraded trigger flow diagram, now fully programmed inside two VME FPGA units. The blue circles are the downstream and upstream signals of the hodoscope bars, the red circles are the vetos. The dashed rectangles represent operations done multiple times as indicated by the numbers beneath.

The signals from the hodoscope bars do not only contribute to the trigger production but they also are transferred to the TDCs. Inside an FPGA programme one signal can be easily used several times without loosing information. For this cause the FPGAs have been programmed to have a direct output of the incoming ToT signals in its C and F ports using two 32-channel LVDS connectors.

Upgrade of the Data Acquisition 6

To enable a faster readout, the DAQ system previously developed by C. Sauerzopf [37] and M. Fleck [39] had to be changed. This included replacing or adding hardware and reprogramming some of the software. This chapter gives an overview of these modifications. The changes in the DAQ system were performed together with Svetlana Chesnevskaya and with support from Hexi Shi.

6.1 DAQ Hardware

As already discussed in chapter 5, for the trigger update one FPGA unit was replaced by two new ones. Additionally, since after the update the digital signals of the hodoscope bars were used instead of the analogue ones, all the digitisers were replaced by a single 128 channel TDC. In Fig. 6.1 pictures of those modules are marked with the used connections. The letters stand for the IFES boards connected (see also Tab. 5.2 for the corresponding channels).
The VME crate additionally houses a VME controller (SIS3104) that connects it to a computer via optical fibre link.

6.1.1 FPGA Settings

The CAEN V2495 general purpose logic units by default come with three LVDS/emitter coupled logic (ECL) 32-channel connectors, where the top two are only for inputs and the bottom one is only for output. There are three empty slots where additional mezzanine boards can be placed. For our purposes in FPGA0 two A395D mezzanines with 8 LEMO 00 channels were used and one A395B for additional 32 LVDS output channels. Our FPGA1 has two A395B mezzanine and one A395D.
The LVDS inputs are used for the creation of coincidence signals for one half of the hodoscope. The one created in FPGA1 is then transferred to FPGA0 where they are connected inside the logic. Other inputs in this unit are the veto signal coming from the SIS and the AD veto. The trigger signal is then distributed to each TDC, the SIS and again to FPGA1. The latter is done to record the trigger signal in the TDCs as well. It is programmed to be transformed to an LVDS signal on several pins in the empty slot on the top right. Additionally a clock signal (CLK) is imported into FPGA1 and transferred to several LVDS outputs to be distributed to the TDCs.
Without alterations, the hodoscope bar signals are put out in the lower connectors of the logic modules and then transferred to TDC2, while the other two TDCs are used only for the fibres.

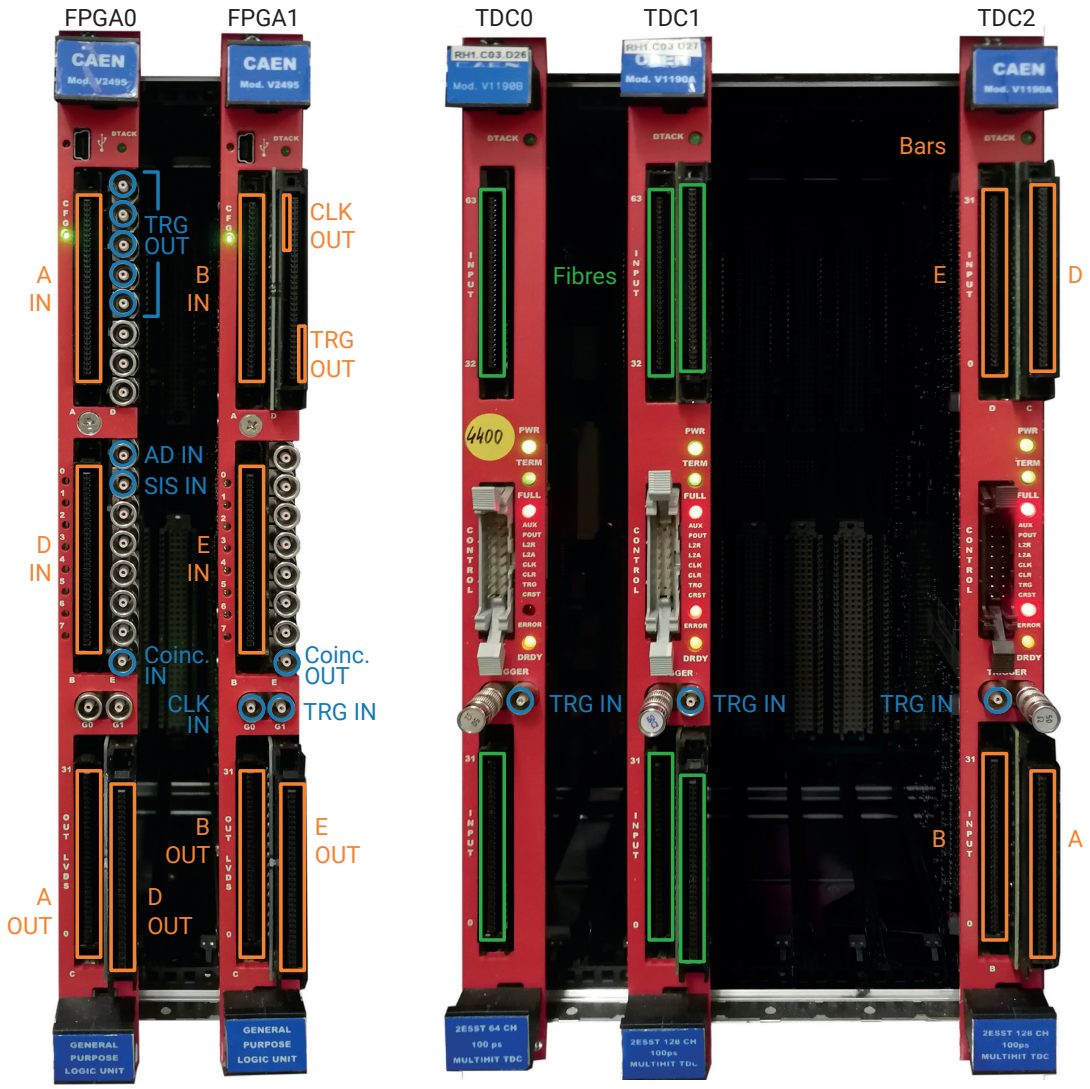

Fig. 6.1.: **Left**: The two FPGA units: in FPGA1 (right) the coincidence signal from the lower half of the hodoscope is produced and then transferred to FPGA0 where the trigger is then produced. **Right**: The 3 TDC units, where units 0 and 1 are for the signals from the scintillating fibres, while unit 2 houses the bar signals. The trigger signal is distributed to the LEMO inputs. The fibre connectors are shown in green, the bar connectors in orange and the used LEMO connectors are marked in blue.

For all LEMO 00 channels the impedance is set by connecting a jumper on the mezzanine either to 50 Ω or to high. For our setup they are all set to the 50 Ω position.

6.1.2 TDC Settings

The CAEN V1190 TDCs are used in trigger matching mode. This means that after receiving the trigger a programmable time window is searched for signals. It can detect either individual leading and/or trailing edges or a leading edge with its corresponding pulse width. In Fig. 6.2 the parameters of the match window are indicated together with a sketch of a signal. For the new setup the edge detection was changed to leading

and trailing edge instead of pair mode (leading edge and pulse width). This was needed because the signals of the hodoscope bars get inverted by the FPGA. Re-inverting the outputs would put a clock-jitter onto these signals. Instead, what the TDC sees as a trailing edge is handled like a leading edge in the analysis and vice-versa.
The detection parameters can be set by sending 16-bit operating codes (opcodes) to the on-board microcontroller. The details on this will be described in section 6.2.

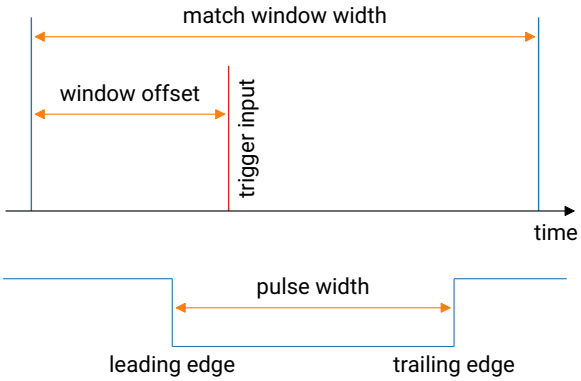

Fig. 6.2.: Top: After receiving a trigger the TDCs look inside their programmed match window for signals. The window is set to have an offset (time before trigger) and a width. Bottom: Example of a signal, where the leading edge, trailing edge and pulse width is marked.

6.2 DAQ Software

The Maximum Integrated Data Acquisition System (MIDAS) is a DAQ system developed at the Paul Scherrer Institute (PSI) and Tri University Meson Facility (TRIUMF) [46]. This software is used for connecting the different components and change the settings of the DAQ hardware over an online database (ODB). The main components of this system are

- `mserver`: a remote server that communicates between the different components and supervises the ODB
- `mlogger`: saves the data from the experiment into files, whose structure is part of MIDAS (.mid)
- `mhttpd`: runs the web server, which allows to communicate using a web browser
- `frontend`: handles the data flow and data transmission, needs to be programmed by the user

The ODB values can be changed either through the web interface or by the command line interface (CLI) `odbedit`.

6.2.1 MIDAS File Structure

A MIDAS file is organised by events, where each trigger signal creates a new one. The data is written in hexadecimal words, which are read from the TDC output buffer. For each event the data is put into so-called MIDAS banks which hold the data. Table 6.1 shows the used banks in the setup.

Tab. 6.1.: Banks used in the produced MIDAS files.

System	Bank	Description
Fibre Detector	TDC0	V1190B Data
	TDC1	V1190A Data
Bar Hodoscope	TDC2	V1190A Data
Frontend	MILT	MIDAS milli second time stamp
	RUNN	Run number

The V1190 data is sent in 32-bit words where the word type is defined by the bits (31-27) to distinguish global header, global trailer, TDC data (header, measurement, error, trailer), global trigger time tag and fillers.

6.2.2 New Frontend

For the new DAQ the frontend was changed to accomodate the additional VME module as well as the omitted ones. The frontend consists of six system functions defined inside the `frontend.cc` and called by `mfe.c`:

- `frontend_init`: initialises all the TDCs and checks their response
- `begin_of_run`: saves the MIDAS time stamp in ms, starts the TDCs and stops the veto in the SIS
- `pause_run`: starts the SIS veto
- `resume_run`: stops the SIS veto
- `end_of_run`
- `frontend_exit`: stops the connection to the VME modules

Inside the frontend also the EQUIPMENT needs to be defined. This is a structure that describes the event trigger type, for which we chose the EQ_POLLED flag (see Listing B.1). This means that in a defined poll time (here 10 ms) the routine will be called as often as possible. A polling function checks whether a variable is true (for us `v1190_DataReady(vme, v1190Adr[0])`) before starting the readout routine `read_tdc_event`.
After the change to polled readout a waveform generator was used to send triggers in different frequencies to the DAQ system. In that way a comparison between the input

rate and the measured rate could be performed and the result can be seen in Fig. 6.3. A trigger rate of up to 300 Hz could be measured without loosing signals.

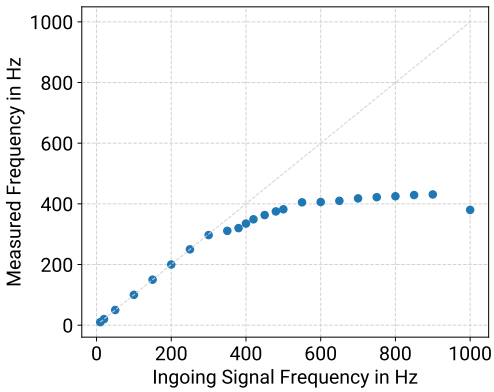

Fig. 6.3.: After changing to polling mode the measured signal rate was compared to the real frequency of a signal produced using a waveform generator.

During `read_tdc_event` first the veto signal from the SIS is started and MIDAS banks for the run number, timestamp and TDCs are initialised, created, filled and closed again. After these processes the veto signal is stopped. This assures that during the whole readout procedure no new event can be triggered and therefore corrupt the data transfer. The whole readout function can be seen in Listing B.2.
Another function – `frontend_loop` – constantly checks the VME module responses and alerts the user if a module is not online.
In the frontend folder the file `v1190.cc` is included where the setup of the TDCs is described. The opcodes are sent to the module by writing

```
value = v1190_MicroWrite(vme, vmeBaseAdress, code);
value = v1190_MicroWrite(vme, vmeBaseAdress, setting);
```

where the used codes and settings (both sent in hexadecimal values) are shown in Tab. 6.2 together with their values converted to decimal numbers.

6.2.3 New TDC Readout Mode

In the TDC each event consists of N_w binary words lead by a global header and ended by a global trailer. After a trigger signal, the event data is loaded into the output buffer. The data transfer can then be done in different ways, two of which have been used with the hodoscope:

- Single data readout: This is event-by-event readout – the data is transferred directly after a trigger signal until a global trailer is sent. The previous DAQ setup used this mode.

Tab. 6.2.: Settings for the V1190 TDCs.

Parameter	Code	Setting	
Trigger Matching	`0x0000`		on
Trigger Window Width	`0x1000`	`0x30`	1200 ns
Trigger Window Offset	`0x1100`	`0xFFF0`	−400 ns
Trigger Subtraction	`0x1400`		on
Extra Search Margin	`0x1200`	`0x0`	off
Reject Margin	`0x1300`	`0x0`	off
Edge Detection	`0x2200`	`0x3`	leading and trailing edge
Resolution	`0x2400`	`0x0002`	100 ps
TDC Header/Trailer	`0x3000`	`0x1`	on
TDC Error Mark	`0x3500`	`0x1`	on
Enable All Channels	`0x4200`	`0x1`	on

- Block transfer (BLT) mode: Using this, N_e events can be transferred at the same time, meaning the system waits until the number is reached before the transfer starts. The event aligned block transfer (BLT) mode makes sure, that no event is split up into two BLT cycles, instead filler words are sent to complete a cycle. For the new DAQ this mode is used, since it enables faster readout.

If the event FIFO (first in - first out) is enabled, the internal FPGA writes the event counter and number of words into its FIFO to ease the readout of the output buffer, since normally the length of an event is unknown. This was also used in the new DAQ system.

Using the new frontend and block transfer mode together with the updated DAQ hardware it was possible to detect events at a rate of over 1 kHz. Compared with the previous data acquisition, this represents an improvement of a factor 20.

Tab. 6.3.: ROOT Leaves created inside the `HbarEventTree`

HbarEventTree	
Leaf	Datatype
midasTimeStamp	UInt_t
midasMilliTimeStamp	Double_t
mixingTimeStamp	Double_t
isMixingSignal	Bool_t
isADPulse	Bool_t
TdcLEInner	Double_t [64]
TdcLEOuter	Double_t [128]
TdcTEInner	Double_t [64]
TdcTEOuter	Double_t [128]
TdcBunchId	Int_t [2][4]
TdcTriggerTime	Int_t [2][2]
TdcTimeTag	Double_t [3]
HodoTdcLEInnerDownstream	Double_t [32]
HodoTdcLEOuterDownstream	Double_t [32]
HodoTdcLEInnerUpstream	Double_t [32]
HodoTdcLEOuterUpstream	Double_t [32]
HodoTdcTEInnerDownstream	Double_t [32]
HodoTdcTEOuterDownstream	Double_t [32]
HodoTdcTEInnerUpstream	Double_t [32]
HodoTdcTEOuterUpstream	Double_t [32]
CUSPRunNumber	UInt_t

6.3 Raw Data Analysis

To pre-analyse the recorded raw data the MIDAS files are converted to ROOT files by the `analyser` programme previously developed by C. Sauerzopf [37] and modified by M. Fleck [39]. To accommodate our modifications, several changes were implemented and are discussed in this section.

A ROOT file generally consists of one or more trees that can have several branches which again divide into multiple leaves. In our case the most important tree is the `HbarEventTree`, which has no branches but multiple leaves, all listed in Tab. 6.3, containing the data.

The `analyser` programme is composed of several files where each one has its own task. The MIDAS file is read in a file that sends the data event by event to another one which transfers it word by word to be divided into the appropriate ROOT leaves. The ROOT trees and leaves are defined by other programs.

With the digitisers in use, the recorded signals were analysed using the `waveformlibrary`, a software library written by C. Sauerzopf [47, 37]. Since no analogue to digital con-

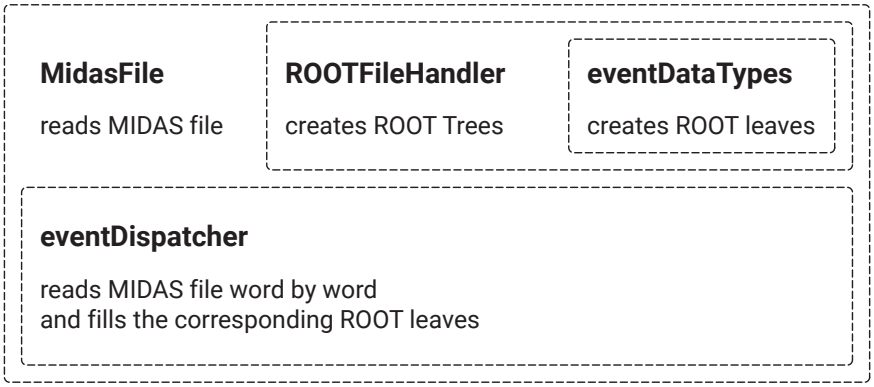

Fig. 6.4.: Scheme of the `analyser` programme, where the intertwined files are shown. The main file is `MidasFile`, which sends the data on to the `eventDispatcher`, where it is filled into the ROOT tree and leaves defined inside the `ROOTFileHandler` and `eventDataTypes`.

verters (ADCs) are in use anymore, this part could be omitted from the programme. Before the upgrade to BLT mode, the data transfer from the TDCs was also done event by event, meaning that each readout cycle corresponded to one event. For the block transfer a new system needed to be implemented in order to reset the event number after each trigger signal and not each readout.

In Fig. 6.4 a scheme of the files used in the `analyser` is shown. The structure of the ROOT file is defined in `ROOTFileHandler`, where for each type of trigger (see Tab. 5.1) a ROOT tree is produced. For the tests conducted in this thesis only the event trigger was used and therefore only the `HbarEventTree` is important. The ROOT leaves for the data are created inside the `eventDataTypes` file, where again depending on the trigger type a specific structure is defined, see again Tab. 6.3.

The `MidasFile` programme reads the .mid file and sends each MIDAS event (defined by one readout cycle) individually on to the `eventDispatcher`. Depending on the event ID the needed ROOT leaves are first cleared and then all the 32-bit words inside the event are decoded. For the previously used `analyser` this was done in two individual programmes which have now been merged into one to easily allow the resetting of the event number after each trigger.

For the "real Hbar events", the event is sent to the `decodeTDC` function which reads the individual words inside the TDC banks. These can be distinguished by the first five bits. In Fig. 6.5 an example of two word types is shown. A measurement word contains one bit which is 0 for leading edges and 1 for trailing edges, the TDC channel number and of course the time of the signal.

The "raw" TDC channels are simply numbered from 0 to 319. Using the function `getHodoChannel` each of these channels is assigned a number which describes the source of the signal. This channel mapping was now extended to also accomodate the additional channels and the whole table can be seen in the appendix Tab. B.3.

With these assigned numbers the data is then saved into a vector which is passed to the function `fillData` (see appendix Listing B.3) where the corresponding ROOT leaf

is filled. After the global trailer of the last TDC is decoded the ROOT tree is filled. Thereby this event is closed and corresponds to a real event unlike the MIDAS event which corresponds to one readout cycle. This is now done until the whole MIDAS event is read out and the process can start again until the end of the whole file.
The resulting ROOT file can now be used for further data analysis.

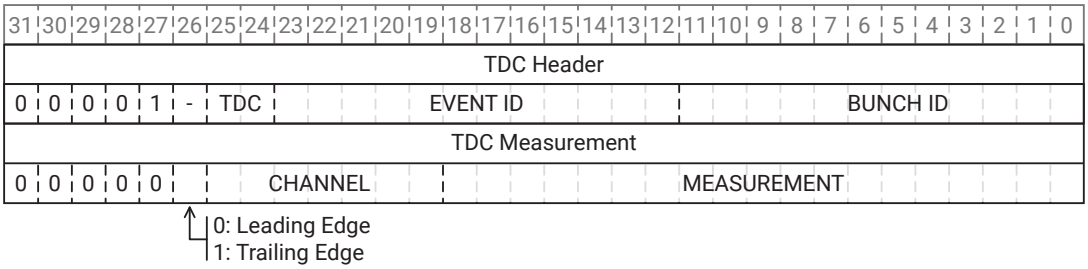

Fig. 6.5.: Examples of the 32-bit words from the TDC output buffer. The header word has two bits (25-24) defining on which TDC chip the signal was measured. The bits (23-12) define an event ID and in the bits (11-0) the bunch ID is saved which is the time of trigger arrival. The measurement word has one bit (26) defining whether it is a leading or trailing edge, the bits (25-19) are the channel number and the signal time is saved in the bits (18-0) [48].

7 Time Resolution Measurements

The time resolution of the hodoscope is important to distinguish cosmic particle events from real annihilation events by their time-of-flight in the detector. In the course of this thesis there have been modifications in the setup discussed in the previous chapters and numerous tests were performed to optimise the time resolution.

7.1 Analogue vs. Digital Signals

Testing the previously used setup with waveform digitisers showed that when going to a trigger rate of 100 Hz the modules already started to heat up and not work properly. This led to omitting the digitisers and switch to the use of TDCs, hence also the migration from analogue to digital time-over-threshold (ToT) signals.
The analysis with the analogue signals was done with offline constant fraction discrimination using the `waveformlibrary`, meaning that for each signal the time at a specific fraction of the amplitude was taken, giving a very constant signal.
The used IFES amplifier boards produce ToT signals using leading edge (LE) discrimination. In Fig. 7.1 these two modes are visualised with two analogue signals with different amplitudes. On the left, leading edge discrimination is applied. A fixed threshold is set and the arrive time is defined as the time where the signal crosses this threshold. This results in different times for different amplitudes. On the right constant fraction discrimination is used. A fraction of the amplitude is fixed (in the example it is 75 %) which forms the threshold. Using this for the different amplitudes the arrive time is the same.

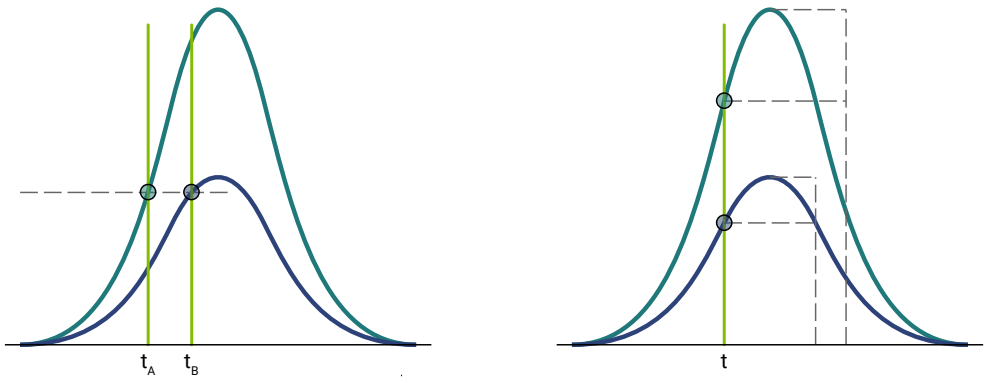

Fig. 7.1.: Left: Two signals with different amplitudes where the arrive times are calculated by leading edge discrimination at a fixed threshold. This results in two times t_A and t_B. Right: Two signals with different amplitudes where the arrive time is calculated by constant fraction discrimination resulting in only one time t.

This means that with the use of the digital ToT signals we need to account for a jitter in the LE times. The following sections present the found solution to this problem.

7.2 Measurements Using Testbars

The hodoscope was shipped from CERN to the Stefan Meyer Institute (SMI) lab in february 2021. Before that, tests with scintillator bars similar to the outer bars of the hodoscope were done in Vienna. In the following, these bars will be called "testbars". The measurements were done with a scintillator including light guides as in the hodoscope setup (called S1) and also without lightguides (called S2). The goal was to find the optimal setup with the best possible time resolution.

7.2.1 Measurements with Radioactive Sources

The scintillator bar "S2" has the same dimensions as the outer bars on the hodoscope but there are no lightguides attached. At each end there are two SiPMs in series, connected to an IFES pre-amplifier board. A metal collimator is used with the ^{90}Sr source to confine the electrons hitting the scintillator to a small spot. This collimator was placed beneath the center of the bar. A smaller scintillator with one SiPM was used as a trigger and positioned on top of the large bar. In Fig. 7.2 a sketch of the setup can be seen, the two SiPMs on the big scintillator bar were called "B1" and "B2", while the one on the smaller bar was called "A".

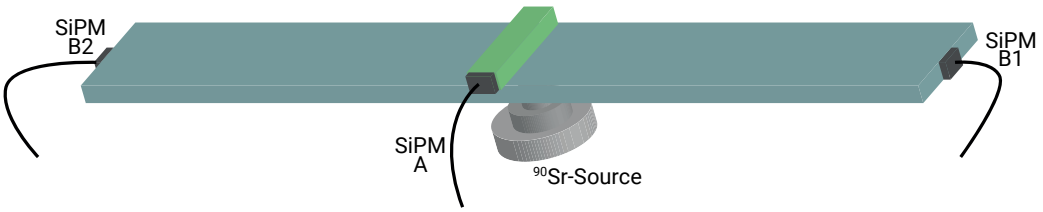

Fig. 7.2.: A sketch of the setup with a radioactive ^{90}Sr source positioned inside a collimator under the long scintillating bar and a smaller scintillator as start counter. Here the testbar has no lightguides attached. At each end of the long bar a SiPM is placed (B1 and B2), the small scintillator has only one SiPM attached (A).

These measurements were done using a LeCroy oscilloscope and the analogue LVDS signals coming from the pre-amplifier boards. These were first sent through a NIM module to convert them to a single ended signal using LEMO cables that can be connected to the oscilloscope. With the measurement setting "dtime@level" the time differences between two signals at either a percentage of the amplitude or a fixed voltage can be determined.
Using the signal from A as a trigger, the time difference between B1 and B2 was

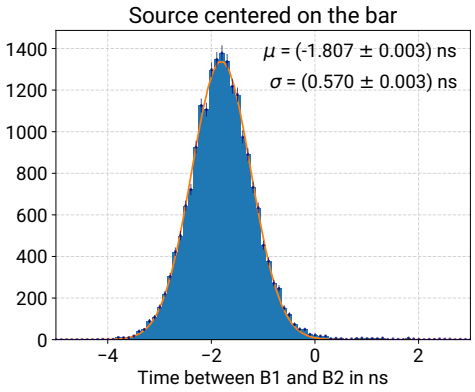

Fig. 7.3.: Histogram of the time differences between the signals at B1 and B2 of the large scintillator bar. The radioactive source was placed in the center of the bar. A Gaussian fit was performed and is shown in orange, where the mean μ and the standard deviation σ are printed in the upper right corner.

measured and saved as a histogram. In Fig. 7.3 one of these histograms is shown and fitted with a Gaussian distribution:

$$f(x) = \frac{1}{\sqrt{2\pi\sigma^2}} \exp\left(-\frac{(x-\mu)^2}{2\sigma^2}\right) \tag{7.1}$$

This histogram shows 19458 events in total, in the top right corner the mean μ and standard deviation σ of the fit is shown. For this measurement the source was placed in the center of the bar, so in principle the signals should arrive at both ends at the same time, meaning $\mu = 0$. The fact that here $\mu = -1.833 \pm 0.003\,\text{ns}$ can be derived from different cable lengths from the SiPMs to the IFES boards.
This measurement was repeated several times with source and trigger at different positions along the big scintillator bar. If the source is placed closer to B1, then the signals there should arrive earlier than at B2 and vice-versa. In Fig. 7.4 each mean and standard deviation of these measurements is plotted against the position on the bar.

The whole procedure was repeated with another scintillator bar identical to S2, where the result is also shown in Fig. 7.4 on the right. In the bottom right corners of the plots the slopes resulting from the linear fits are printed and it can be seen that with $k = (0.146 \pm 0.004)\,\text{ns/cm}$ and $k = (0.148 \pm 0.001)\,\text{ns/cm}$ these are equal within their uncertainties.

Next, these tests were performed using the digital ToT signals produced by the IFES amplifier boards. When connecting these boards to a computer via USB, the on-board Arduino Leonardo can be controlled to set the wanted threshold.
For the following tests the setup with the ^{90}Sr and the smaller scintillator with SiPM A was the same. The digital signals were first sent to an FPGA unit where a logic had been programmed to send a trigger signal to a TDC as soon as there was a signal on the small bar. The recorded data was then transformed to a ROOT file, where it could be analysed.

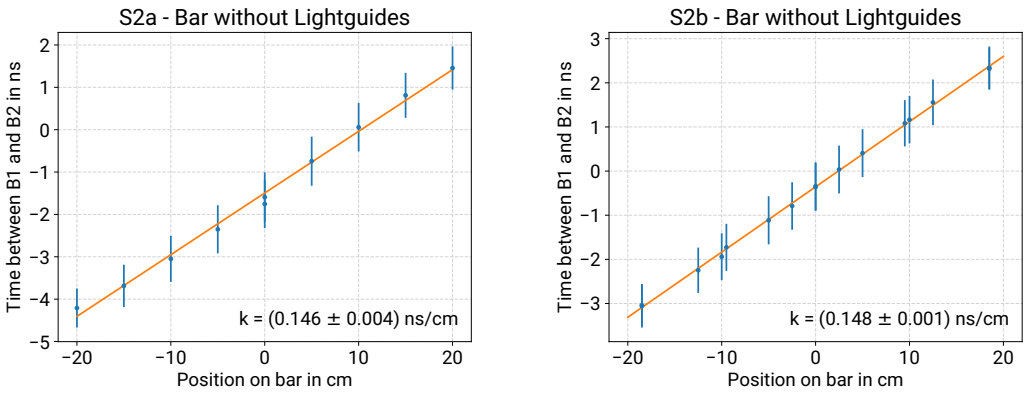

Fig. 7.4.: The means of the time differences between B1 and B2 plotted against the position of the source along the bar, where 0 cm is the middle. The y-errorbars show the standard deviations. The orange line shows a linear fit, where the resulting slopes for the two similar scintillator bars are printed in the bottom right corners.

Depending on the amplitude and therefore also width of a signal, the rise times of the analogue signals vary. This can be seen when plotting the timing against the time-over-threshold, as the profile of this correlation is not horizontal. To counter-act this effect a so-called "slew correction" can be performed. This means fitting the profile of the two-dimensional histogram with a function and then correct this "slew" using the fit parameters.
In our case the used function was of exponential form:

$$f_{slew}(x_{\mathrm{ToT}}) = A + B \cdot \exp\left(-C \cdot x_{\mathrm{ToT}}\right) \tag{7.2}$$

The timing $t = t_B - t_A$ was then corrected to

$$t_c = t - B \cdot \exp\left(-C \cdot x_{\mathrm{ToT}}\right). \tag{7.3}$$

In Fig. 7.5 on the left side these two-dimensional histograms can be seen for both B1 and B2. Signals with widths of under 30 ns were cut. The orange line shows the fitted slew function which is then used to obtain the slew corrected histogram below. On the right the y-projections of these histograms are plotted, which show the distribution of the (corrected) timings including a Gaussian fit.
The standard deviations of these Gaussians are "slimmed" by the slew correction:

$$\sigma_{t\,\mathrm{B1}} = (3.696 \pm 0.004)\,\mathrm{ns} \qquad \sigma_{t_c\,\mathrm{B1}} = (2.745 \pm 0.004)\,\mathrm{ns}$$
$$\sigma_{t\,\mathrm{B2}} = (3.607 \pm 0.004)\,\mathrm{ns} \qquad \sigma_{t_c\,\mathrm{B2}} = (3.047 \pm 0.004)\,\mathrm{ns}$$

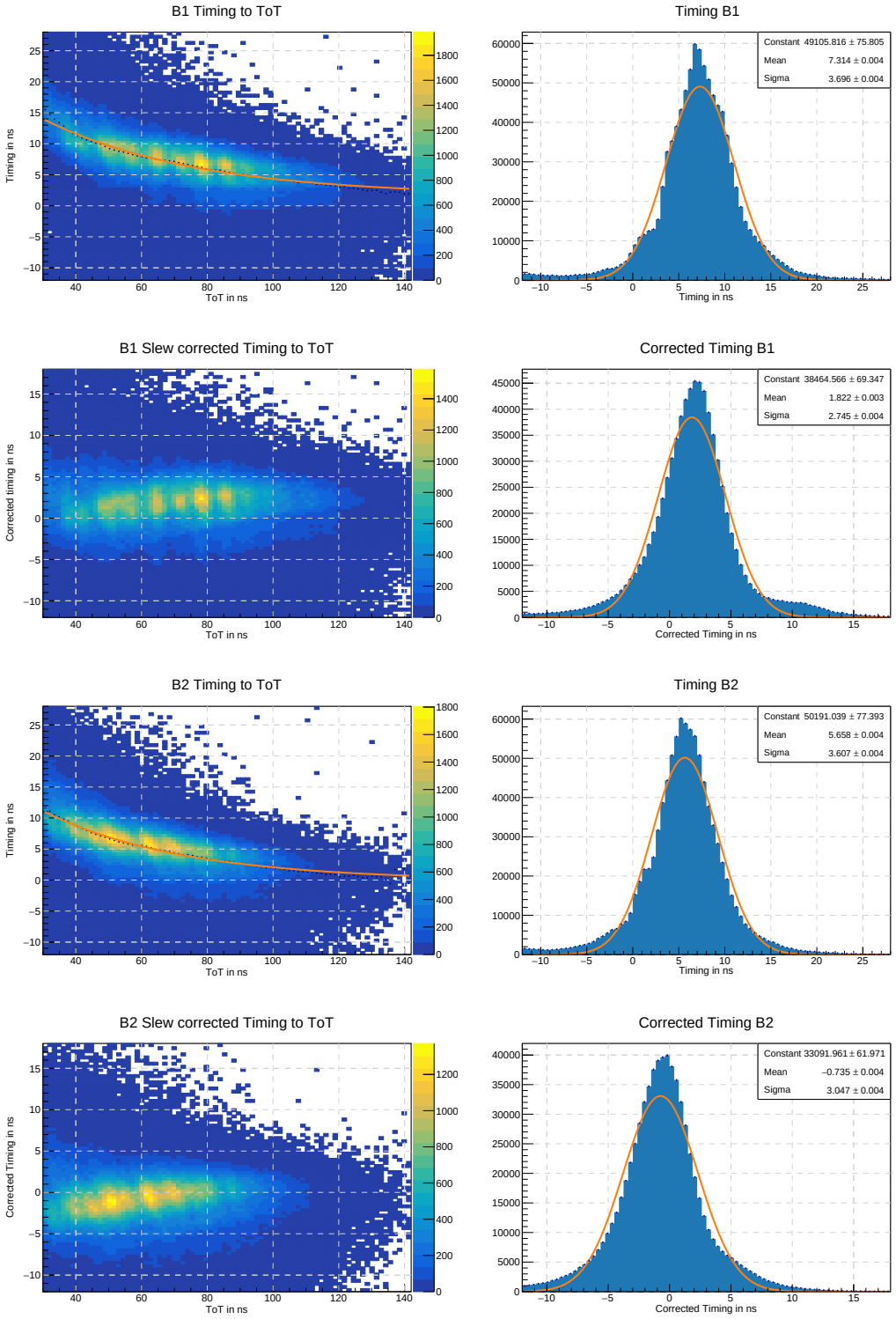

Fig. 7.5.: Graphs of the slew correction for B1 (upper 4) and B2 (lower 4). The timing to ToT correlations (upper left) are shown with their profiles (dark blue dots) which are then fitted with the slew function (orange line). The slew corrected timing to ToT correlations is plotted below. On the right the timing and corrected timing histograms are shown together with Gaussian fits (orange line).

7.2.2 Measurements with a Pulsed Laser

To test weither the signal height has influence on the time resolution a new setup with a pulsed laser (404 nm wavelength) instead of the radioactive source was built. In this setup the start signal of the small SiPM A was replaced by the laser pulse signal. Between the laser and the scintillator bar an absorptive filter and a top-hat diffuser was placed to lower the intensity of the beam and broaden it. A sketch of this can be seen in Fig. 7.6.
A "Thorlabs NDC-50C-4M" was used, which is a variable neutral density filter with angular graduations. The optical density OD varies between 0.04 and 4.00, allowing to manipulate the transmission T of the beam with [49]

$$T = 10^{-OD} \tag{7.4}$$

Using this, the beam intensity and therefore the amplitudes of the produced signals, could easily be changed – this was not possible using the radioactive source.

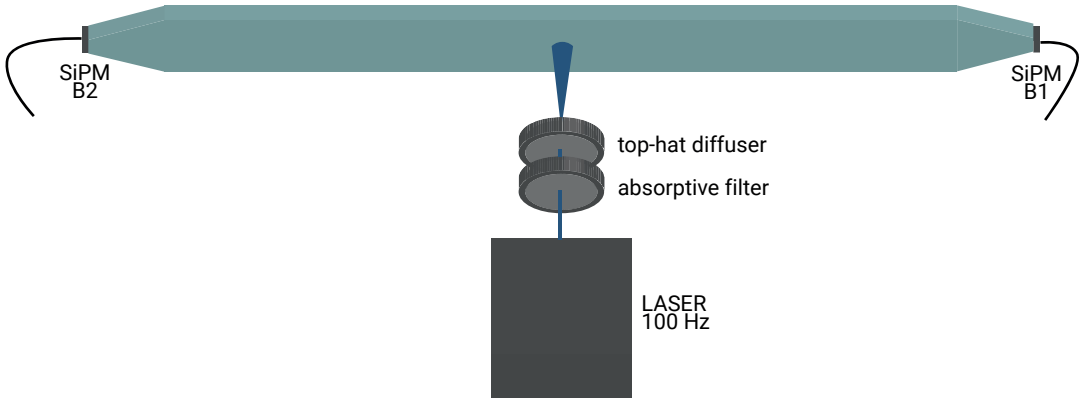

Fig. 7.6.: A sketch of the setup with a pulsed laser positioned in front of the scintillator bar. The laser beam first goes through an absorptive filter to lower the intensity and then through a top-hat diffuser so the beam has a diameter of ≈ 5 mm.

First, it was tested if the timing resolution is different for a bar with lightguides (S1) and without lightguides (S2). For both the optical density of the filter was set to $OD \approx 2.4$. For S1 the resulting amplitudes were in the range of $80 - 110$ mV, for S2 between $500 - 700$ mV. We therefore see that the attached lightguides minimise the light reaching the SiPMs significantly.

Tab. 7.1.: Threshold settings for both SiPMs on S1 and S2.

	S1	B1	B2	S2	B1	B2
Threshold		≈ 60 mV	≈ 40 mV		≈ 130 mV	≈ 120 mV
Mean ToT		≈ 40 ns	≈ 40 ns		≈ 100 ns	≈ 100 ns

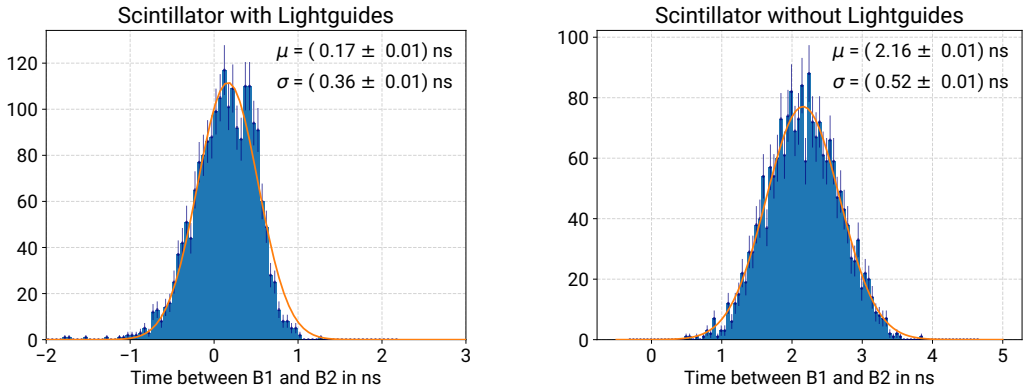

Fig. 7.7.: Histograms of the time differences between the signals at B1 and B2 of a bar with lightguides (left) and without lightguides (right). The orange lines show Gaussian fits of the distributions, where the mean μ and standard deviations σ are shown in the top right corners.

In Tab. 7.1 the set threshold for each SiPM together with its mean time-over-threshold are listed. Using the oscilloscope the mean times between the signals at B1 and B2 were then measured using the digital signals. In Fig. 7.7 the resulting distributions are shown together with their Gaussian fits. The resulting parameters are

$$\mu_{\Delta t\,\mathrm{S1}} = (0.17 \pm 0.01)\,\mathrm{ns} \qquad \mu_{\Delta t\,\mathrm{S2}} = (2.16 \pm 0.01)\,\mathrm{ns}$$
$$\sigma_{\Delta t\,\mathrm{S1}} = (0.36 \pm 0.01)\,\mathrm{ns} \qquad \sigma_{\Delta t\,\mathrm{S2}} = (0.52 \pm 0.01)\,\mathrm{ns}.$$

The mean values are different because of asymmetric cable lengths on the scintillator with lightguides. As the standard deviation is smaller for S1, we assume that the bars with lightguides provide better time resolution despite the lower amplitudes. The same conclusion could also be drawn from the timings t of the signals, where the standard deviations were:

$$\mathrm{S1}: \quad \sigma_{t\,\mathrm{B1}} = (0.289 \pm 0.004)\,\mathrm{ns} \qquad \sigma_{t\,\mathrm{B2}} = (0.211 \pm 0.004)\,\mathrm{ns}$$
$$\mathrm{S2}: \quad \sigma_{t\,\mathrm{B1}} = (0.394 \pm 0.007)\,\mathrm{ns} \qquad \sigma_{t\,\mathrm{B2}} = (0.39 \pm 0.01)\,\mathrm{ns}$$

As discussed before in section 7.1 there is a jitter in the LE times due to the leading edge discrimination in the IFES boards. In Fig. 7.8 on the left there is a sketch of two analogue signals with different amplitudes and their times over a fixed threshold are indicated. Due to the difference in rise times, the ToT signal is not produced at a certain fraction of the amplitude. If the signals are produced with SiPMs operated in saturation, as seen in the figure on the right, the amplitude of all signals is maximal ($\approx 800\,\mathrm{mV}$). By taking the LE times at a specific threshold voltage, the signals are more constant due to the minimal rise times.
After setting the optical density to $OD \approx 1.03$ the signals on the S1 bar were in saturation, this means that the maximal amplitude of about 800 mV is reached. With this configuration a measurement with digital signals sent to the FPGA and read out

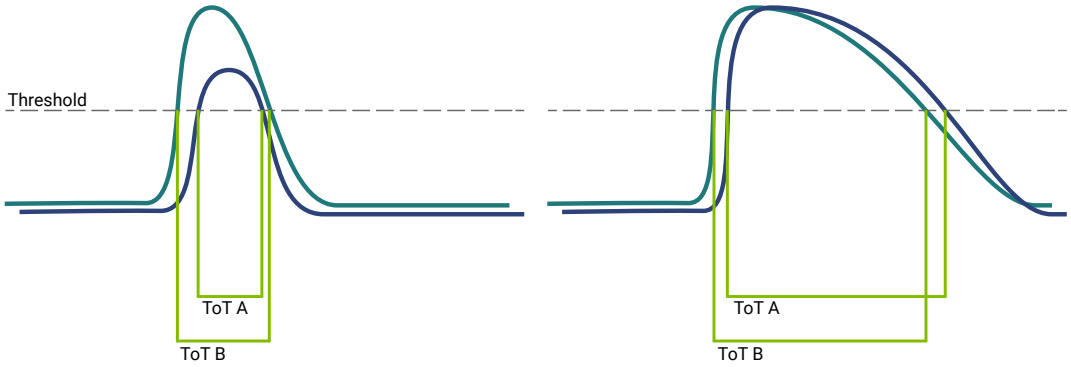

Fig. 7.8.: A sketch of analogue signals not in saturation (left) and in saturation (right). For a threshold fixed at a certain voltage (y-axis), the leading edge of the ToT signal depends on the rise times of the signals. If the amplitude is higher, the rise time is shorter. If the signals are all in saturation the jitter in the leading edge can be avoided.

by a TDC was performed. As can be seen in Fig. 7.9 on the left, the correlation between the ToT and the timing was already nearly horizontal and no slew correction was performed. The graphs on the right show the timing histograms for B1 and B2, which are again fitted with a Gaussian distribution showing rather narrow standard deviations of only

$$\sigma_{t\,\mathrm{B1}} = (0.07924 \pm 0.00005)\,\mathrm{ns} \qquad \sigma_{t\,\mathrm{B2}} = (0.07468 \pm 0.00005)\,\mathrm{ns}.$$

This measurement was then repeated for several positions. The distance between the laser and the scintillator stayed the same but it was positioned at different points along the bar. As already shown for the measurement with the ^{90}Sr source (Fig. 7.4) the mean time differences between B1 and B2 were again plotted against the positions.
For all the different positions the mean value of the standard deviations is 0.082 ns. Fig. 7.10 shows the data together with a linear regression, where the resulting slope is $k = (0.124 \pm 0.005)\,\mathrm{ns/cm}$ and the offset is $d = (0.94 \pm 0.04)\,\mathrm{ns}$.

When rearranging the linear function $\Delta t = x \cdot k + d$ to $x = (\Delta t - d)/k$ the maximal uncertainty value for the position x is 1 cm. So we can assume that with this time resolution we have a position resolution of about ± 1 cm standard deviation.
Compared with the previous results from [50] where a position resolution of 7.3 cm at full width at half maximum (FWHM) – 3.1 cm at standard deviation – was achieved, this would be an improvement by a factor of 3.
In the following section the whole hodoscope setup was tested to see whether a similar resolution could also be achieved there.

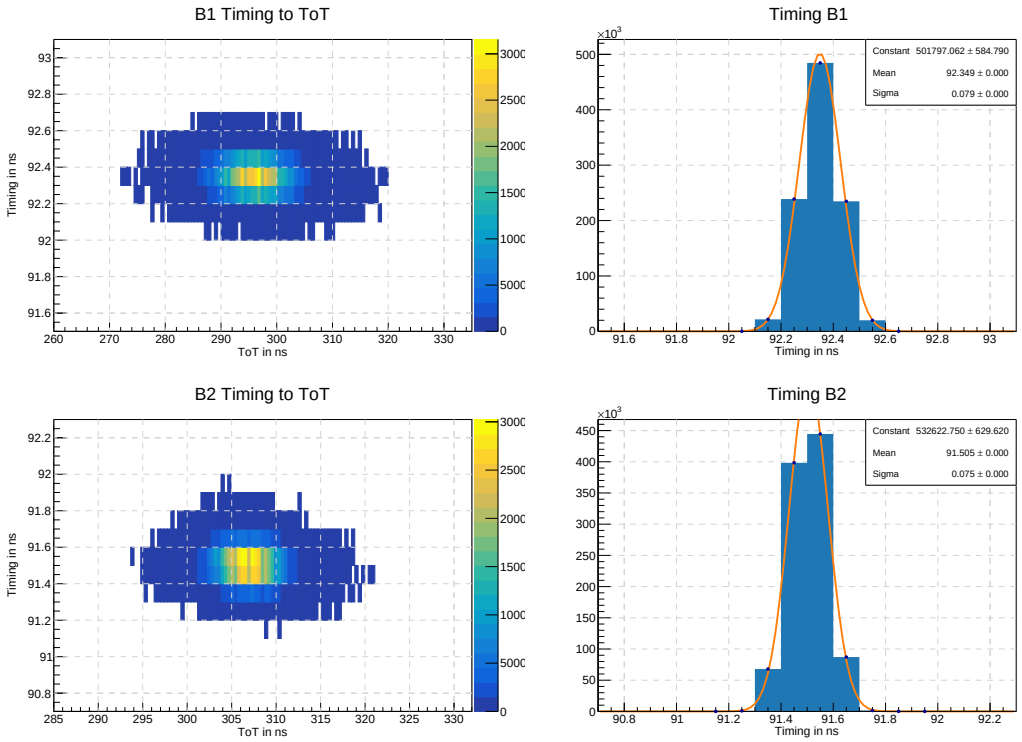

Fig. 7.9.: **Left:** Timing to ToT correlations for B1 (top) and B2 (bottom). **Right:** Histogram sof the timing for B1 (top) and B2 (bottom), each fitted with a Gaussian distribution, where the fit parameters are shown in the top right corner. The time resolution of the used TDC is only 0.1 ns. This is the reason for the broad binning in the histograms.

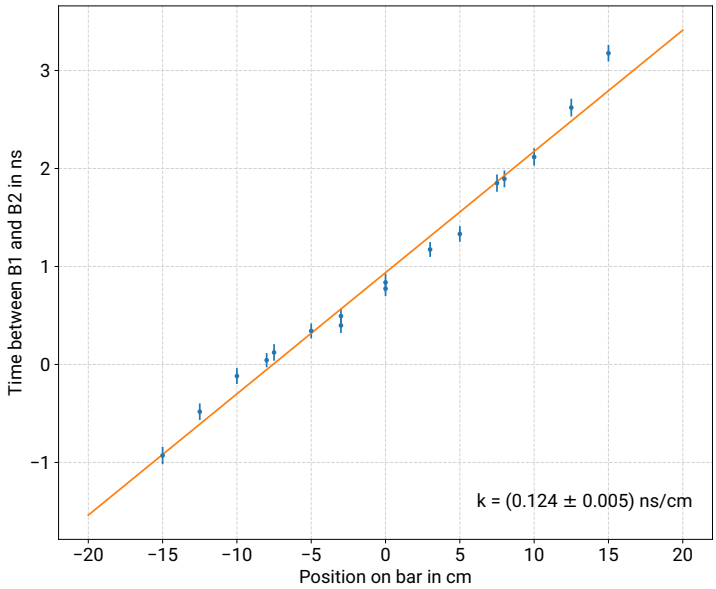

Fig. 7.10.: The means of the time differences between B1 and B2 plotted against the position of the laser along the bar, where 0 cm is the middle. The y-errorbars show the standard deviations. The orange line shows a linear fit, where the resulting slope is $k = (0.124 \pm 0.005)\,\mathrm{ns/cm}$.

7.3 Testing the Hodoscope

To test the time resolution of the hodoscope using the whole DAQ system the usage of radioactive sources was not possible since the energies of the particles are too small to penetrate several layers. Therefore most of the tests were done using cosmic particles. This introduced the problem that the position of the hit along the bars is unknown since cosmic particles are equally distributed. Testing the setup with a laser as done with a testbar (see subsection 7.2.2) was also not possible since all the elements are wrapped light-tight.
This section discusses all tests that were performed to gain information on the time and position resolution of the adapted hodoscope setup.

7.3.1 Measurements with Radioactive Sources

Particles from a radioactive source can only penetrate a single layer of the hodoscope. To still trigger the DAQ, the logic had to be adapted to not require a signal coincidence of the outer and inner bar layer, but only of the two ends of a bar.
With this modified FPGA trigger programme installed, a measurement with the ^{90}Sr source was performed at 5 different positions along bar 0 of the outer hodoscope.

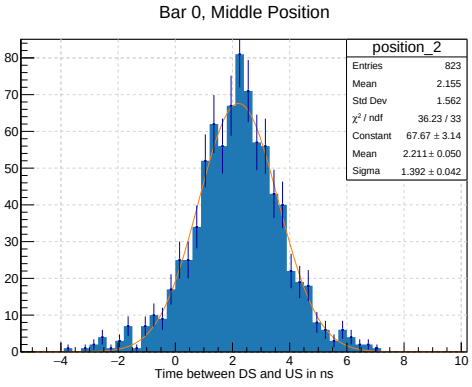

Fig. 7.11.: Time difference histogram between downstream and upstream leading edges. The measurement was done using a radioactive source positioned at the center of the outer scintillator bar 0. The standard deviation acquired by the Gaussian fit is $\sigma = (1.39 \pm 0.04)$ ns.

Fig 7.11 shows the result for the central position while Fig. 7.12 shows all of them together with a linear fit. The standard deviations of the (downstream - upstream) time difference histograms are between 1.25 ns and 1.79 ns. These relatively large values are attributed to the SiPMs not being operated in saturation as this is not possible with the used amplifier boards.
To again confirm that this is the reason, a quick test was conducted using two different IFES boards with different signal amplification factors. The source was placed in the center of a bar and the time differences of the leading edges of downstream and

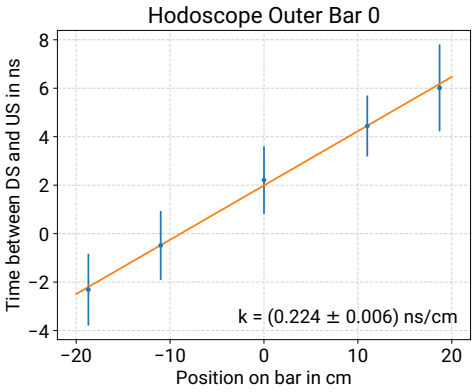

Fig. 7.12.: The means of the time differences between downstream and upstream leading edges is plotted against the position of the source along the bar, where again 0 cm is the middle. The y-errorbars show the standard deviations. The orange line shows a linear fit, where the resulting slope is $k = (0.224 \pm 0.006)\,\mathrm{ns/cm}$.

upstream signals were recorded using the oscilloscope. The normalised histograms are shown in Fig. 7.13 together with their Gaussian fits. For the original amplifier board the standard deviation $\sigma = (2.28 \pm 0.02)\,\mathrm{ns}$ is larger than for the board with the higher amplification ($\sigma = (0.71 \pm 0.02)\,\mathrm{ns}$) by a factor of ≈ 3.

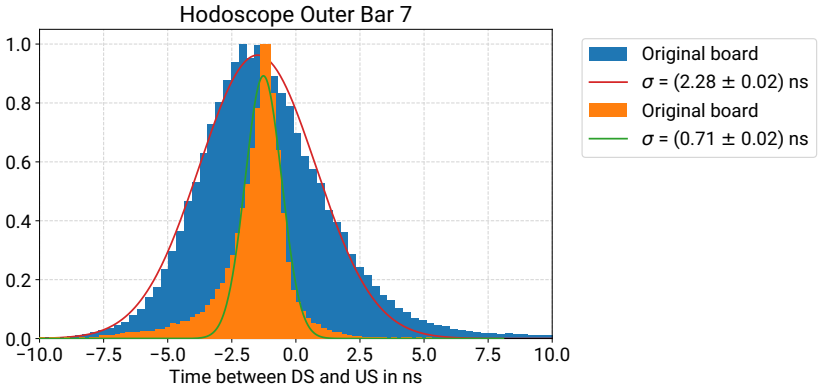

Fig. 7.13.: Normalised histograms of the time differences between downstream and upstream leading edges. The blue distribution shows the data recorded for the original amplifier board and the orange data was detected using a board with higher amplifications and therefore SiPMs nearly in saturation. For both a Gaussian fit was performed where the standard deviations σ are printed on the right.

7.3.2 Measurements with Cosmic Particles

The only available particle source with energies high enough to transverse the whole detector system and by that trigger the DAQ, is cosmic rays. These should hit the hodoscope bars in a uniform distribution.

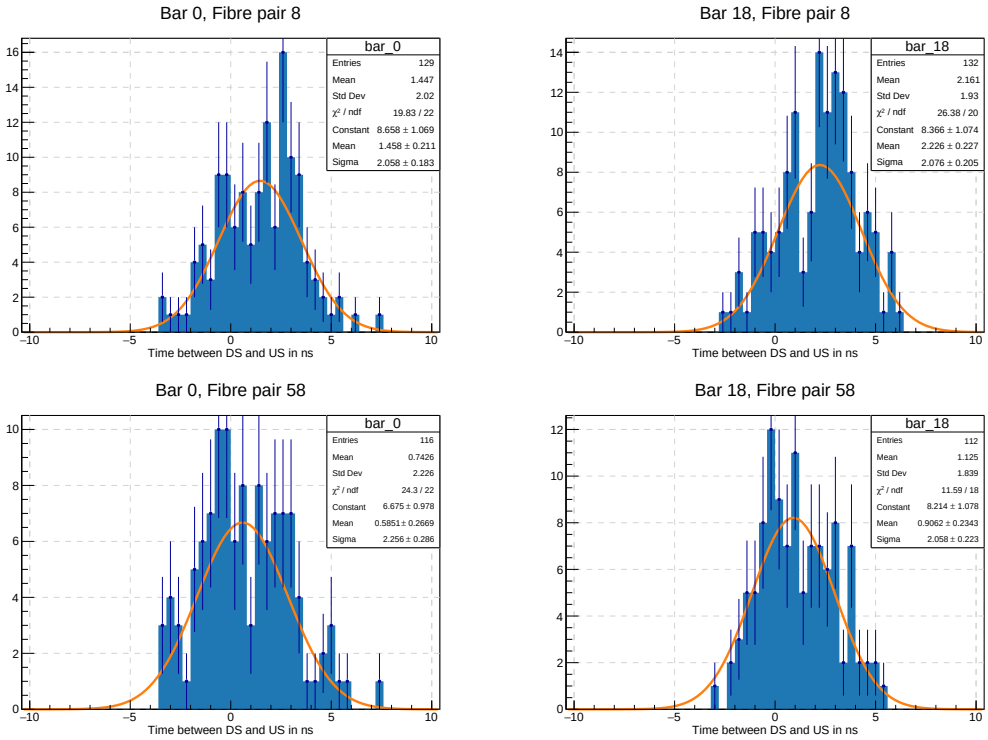

Fig. 7.14.: Example of the time difference histograms when looking at fibre coincidences for the two bars 0 and 18. The two fibre pairs 8 and 58 (corresponding to inner fibre 8 and outer 27 or inner fibre 58 and outer 77) were chosen as their positions are 20 cm apart.

Position Resolution via Fibre Coincidences

To obtain the position of the cosmic hit, offline data analysis was used assuming particles transversing the detector vertically. If a particle hits both the inner and outer fibre at a specific position along the z-axis, the hit should also be at that position along the bars. In the analysis this was done by plotting the leading edge time differences of each bar only if there was a signal on inner fibre n and outer fibre $n + 19$. Looping over the inner fibres ($0 \leq n \leq 63$) and plotting the means of the time differences against the fibre position, it was assumed that it would follow the same linear function as seen in Fig. 7.12.

The rate of cosmic particles transversing the detector in a way to trigger the DAQ is between 1 and 3 Hz and the events where a cosmic travels vertically through the detector are even more rare. In one run lasting for over a week, in total 1 519 614 events were detected, but for each fibre coincidence the individual bars had on average only about 93 counts. Even with as little counts as that, it could be seen that the distributions of time differences were wider than with the testbar.

In Fig. 7.14 the time difference histograms are shown for bars 0 and 18 in coincidence with the inner fibres 8 (outer 27) and 58 (outer 77). The fibre pairs are 20 cm apart but it can be seen that the Gaussian mean values lie within their standard deviations. This long run was performed while the top four scintillator bars (8-11) were not attached

to the hodoscope. The mean of all acquired standard deviations comes to (2.6 ± 0.9) ns. Fig. 7.15 shows these measurements for all used bars. The y-errorbars show the standard deviations, while the orange lines are linear fits. In addition to the larger standard deviations one can see that the slope of those linear fits is smaller than previously measured. The mean of all obtained slopes is (0.049 ± 0.016) ns/cm, which does not corrrespond to the slope found with the radioactive source of (0.224 ± 0.006) ns/cm (Fig. 7.12).
Even with the current IFES amplifier boards, cosmics mostly produce signals in saturation. This means that the distributions should be more similar to the ones aquired with the testbar (Fig. 7.9) than to those resulting from the use of radioactive source (Fig. 7.11), but the actual results have an even worse resolution.
The reason for these results could not be savely determined. One assumption was that the fibres were not working properly but testing the bars and fibres seperately showed viable results.
Fitting the time differences for all signals on one bar without fibre coincidences results in similar distributions with a mean standard deviation of (2.5 ± 0.2) ns. This would support the assumption that there is some problem with the data alignment between fibre events and bar events.

Cosmics Time of Flight

Another way of checking the time resolution is to measure the time a cosmic particle takes to transverse the detector. For this first the mean time m_k on each bar k was calculated as

$$m_k = \frac{1}{2}(t_{k,u} + t_{k,d}) \tag{7.5}$$

where $t_{k,u}$ is the upstream leading edge time and $t_{k,d}$ is the downstream leading edge time. To get the correct mean times m'_k the trigger should be subtracted from each leading edge:

$$m'_k = \frac{1}{2}(t_{k,u} + t_{k,d}) - t_{trg} \tag{7.6}$$

The trigger signal itself is not recorded on TDC2 yet, but by taking the mean time differences Δm_{ij} for two opposite bars i, j this was avoided since t_{trg} cancels for $m'_i - m'_j$.

$$\Delta m_{ij} = m_i - m_j = m'_i - m'_j = \frac{1}{2}(t_{i,u} + t_{i,d} - t_{j,u} - t_{j,d}) \tag{7.7}$$

To get the time of flight between two opposite bars the mean time differences between bars i and $j = i + 16$ (for $0 \leq i \leq 15$) were calculated. This was done with the same big dataset mentioned before, where bars 8-11 were not connected. In Fig. 7.16 Δm_{ij} was plotted for all available bars together with their Gaussian fits. The mean of the acquired standard deviations here is (2.3 ± 0.3) ns.

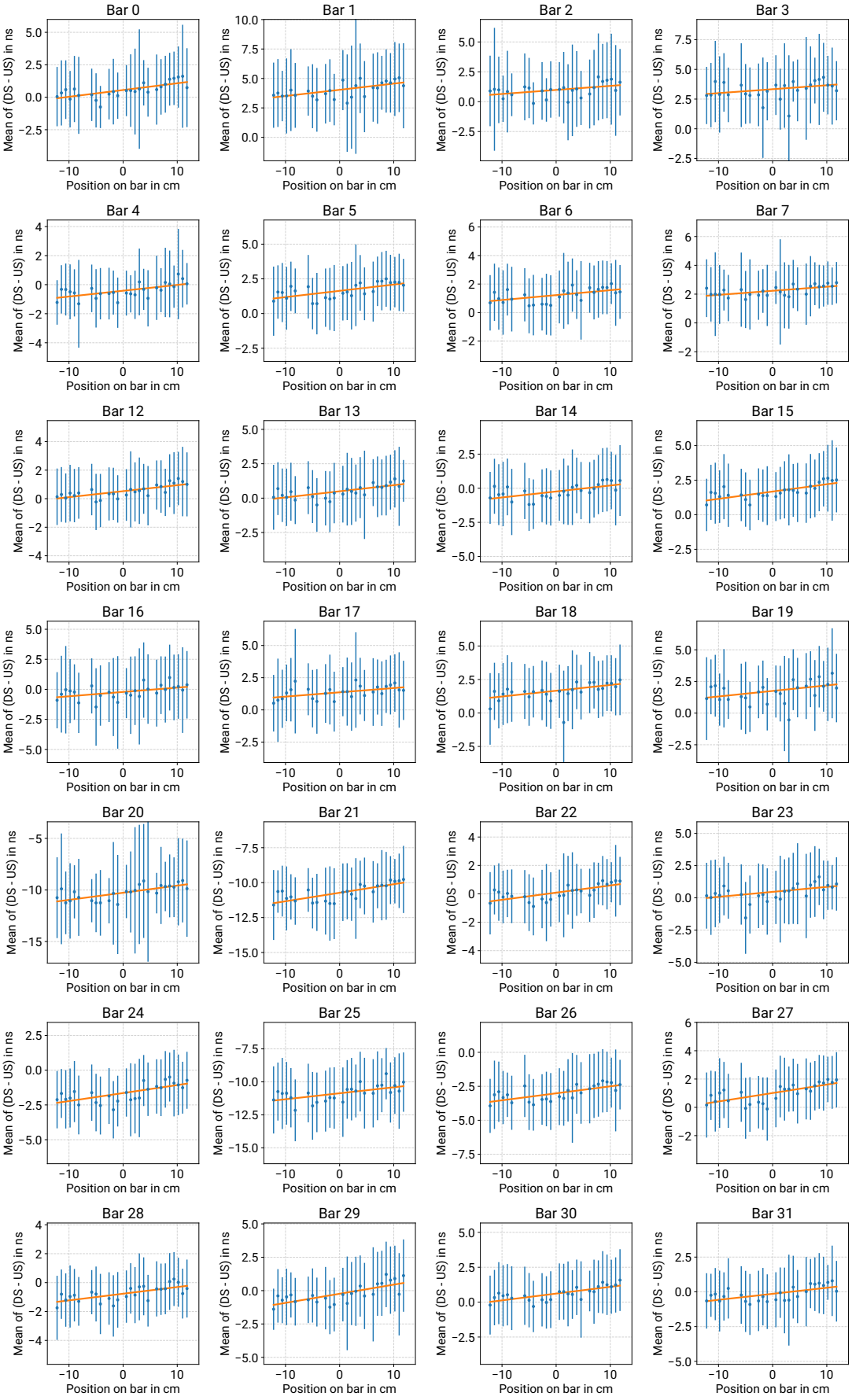

Fig. 7.15.: For several fibre pairs the time differences of upstream and downstream SiPMs on the bars were measured and here plotted against the fibre position along the bars. The y-errorbars show the standard deviations and in orange linear fits are shown.

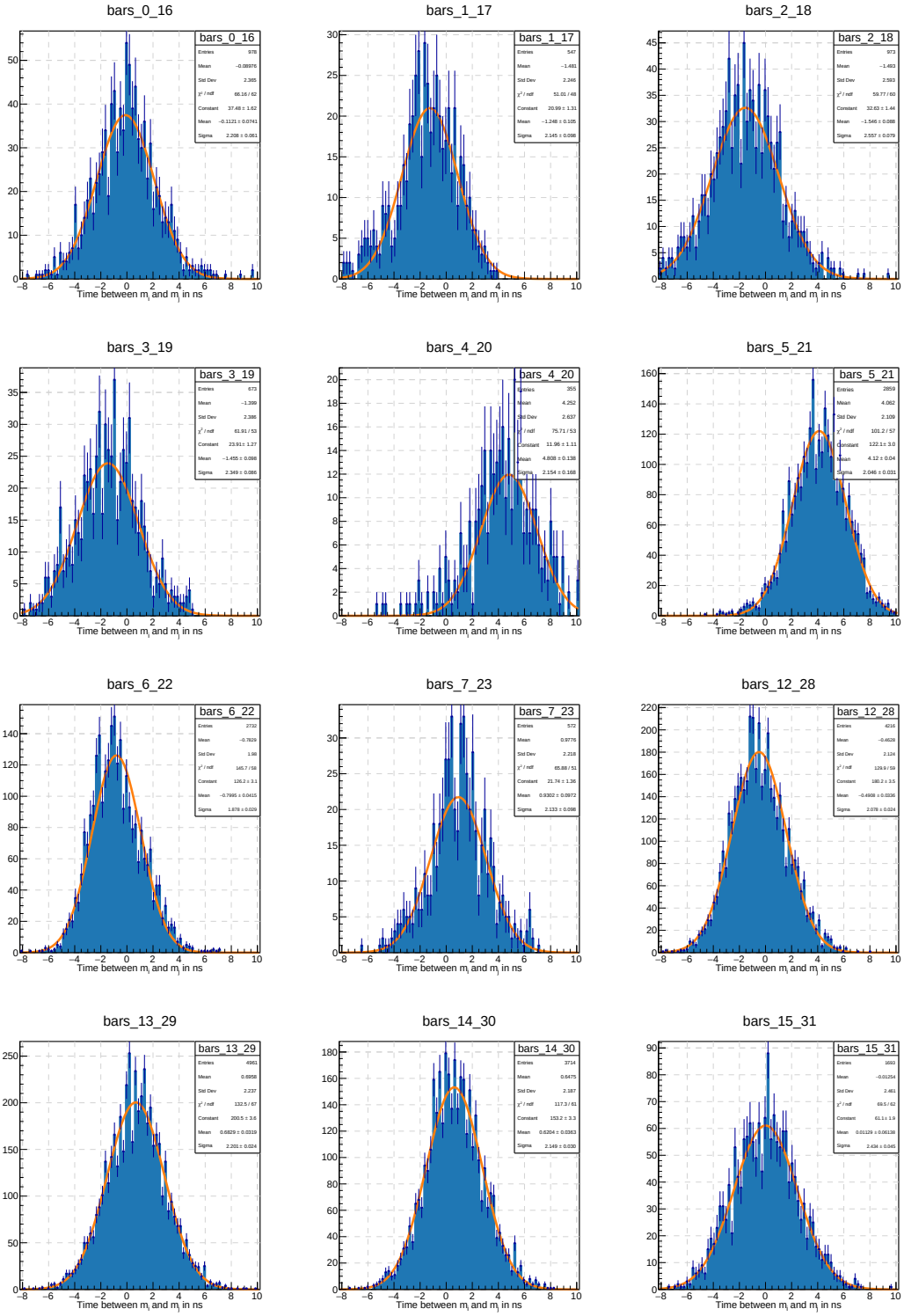

Fig. 7.16.: The mean time differences Δm_{ij} for two opposite bars i and j (the individual titles are bars_i_j).

7.4 Importance of Time Resolution

The time resolution of the antihydrogen detector is mostly used to distinguish annihilation products from cosmic particles. This is done by checking the time-of-flight of a particle inside the detector and discriminating particles produced inside the detector from particles entering it from the outside.
The importance of background subtraction depends on the rate of antihydrogen annihilation events. The higher the rate of $\overline{\mathrm{H}}$ events, the smaller the fraction of cosmic background. If for future runs the annihilation rate really reaches the aimed for 1 kHz, the time resolution on the bars is less important as the cosmic events have a negligible fraction.
Nonetheless, the goal is still to reach a higher resolution. To achieve this several upgrades will still need to be performed, which will be discussed in the outlook section 8.2.

8 Summary and Outlook

8.1 Summary

The goal of this thesis was to upgrade the ASACUSA antihydrogen detector in a way to allow data acquisition at a higher rate. The reason for this was that a new mixing scheme will be applied in which up to 1000 antihydrogen atoms should reach the detector in one second.
This goal was achieved by the use of only digital time-over-threshold signals instead of analogue signals together with waveform digitisers. To achieve this several changes were performed:

- One additional 128-channel TDC was added to the DAQ hardware to record the hodoscope bar signals while the five previously used digitisers were omitted.
- A new MIDAS frontend with polling function was written, which allowed data rates up to 300 Hz without losses.
- To increase the possible data taking rate even more, the TDCs were switched to block transfer mode. By doing that events at a rate of over 1 kHz can now be detected. This also lead to changes in the `analyser` function to keep the events aligned to the trigger signals.

The NIM modules used to produce the trigger signal were all replaced by two VME FPGA units. The logic was programmed to produce the trigger when a signal is present on two ends of a bar and on at least one inner and one outer layer.
A second goal was to optimise the time resolution of the hodoscope bars. To achieve this a number of tests were performed using a testbar equal to the scintillator bars used on the hodoscope. Because of the switch to digital time-over-threshold signals produced by leading edge discrimination, there was a jitter in the signals and a way to avoid that needed to be found. The conclusion was that when the SiPMs are operated in saturation, the jitter in the leading edges is minimal and therefore a time resolution of under 100 ps standard deviation could be obtained with a laser.
These results from the testbar could not be confirmed with the whole hodoscope setup due to several complications. For one, there is no available particle source that can penetrate more than one layer of the detector except for cosmic particles. For the tests with a radioactive source the trigger had to be changed and the SiPMs could not be operated in saturation due to the amplification on the IFES boards. This resulted in a time resolution of over 1.25 ns standard deviation.
For the performance of measurements with cosmic particles the position of the hit along the bar was not known. By looking at the coincidences of signals on one inner fibre and

the corresponding outer fibre, it was not possible to achieve the same time resolution as with the testbar. The same observation holds for the time-of-flight of cosmic particles in the detector. A time resolution of only (2.3 ± 0.3) ns standard deviation could be achieved.

The following outlook discusses the steps that have to be taken to reach the needed time and position resolution to distinguish cosmic particles from annihilation products.

8.2 Outlook

In the course of this thesis it became clear that the hodoscope is still in need of several upgrades to be fully operational until the next ASACUSA beamtime. Some of these points were already mentioned, like the need of higher signal amplification, others will be introduced in the following.

Amplification

As discussed in subsection 7.3.1 the amplification on the hodoscope bar's IFES boards should be increased to mostly receive signals in saturation. Only then the maximum potential in time resolution can be reached with leading edge discrimination.

Trigger readout

Even though all the TDCs receive the same clock trigger, one cannot be sure that there is no jitter due to different signal alignments. This can only be accounted for by also recording the trigger signal in each unit and then subtracting it from all of the leading edge times.
At the moment the cable distribution on the TDCs does only allow to measure the trigger signal on TDC0. For that reason a possible clock jitter on the other two units cannot be accounted for when subtracting the trigger time. This could be an additional reason for the bad time resolution measured on the hodoscope bars. The updates discussed in the next subsections will provide a possibility to allow trigger recording on each TDC unit since an additional unit will be purchased.

Once the trigger signal is distributed to each module and the amplification is increased, a cable length correction factor can be measured using the mean times.

Replacement of the Fibres

Since the position coincidence with the fibres was not working as expected they will be replaced completely by two new layers of scintillating tiles. On each octagon side of 4 bars 15 tiles will be placed in a 90° angle as seen in Fig. 8.1. Each tile will be read out on one side by two 3x3 SiPMs connected in series. This means in total 240 (15 tiles

on the 8 sides for the outer and inner layer) channels that need to be read out, so an additional CAEN V1190A TDC will be used together with the one already in use for the fibres. The inner tiles will have a size of $(80 \times 20 \times 5)$ mm and the outer tiles will be $(140 \times 30 \times 5)$ mm. By looking at the coincidences between a bar and a tile the resulting position resolution should be at least 30 mm along the outer bars and 20 mm along the inner bars.

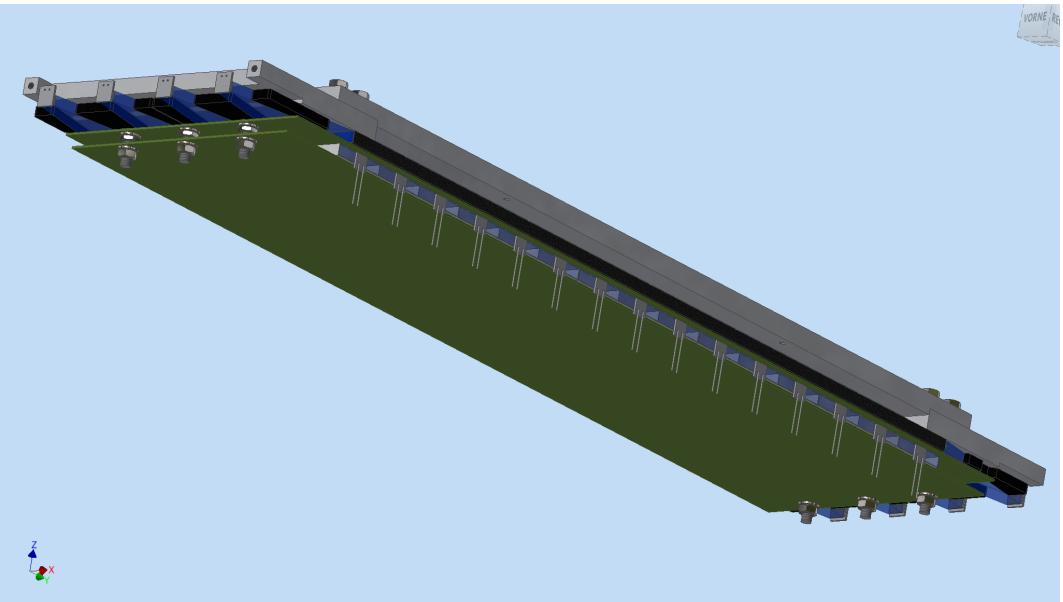

Fig. 8.1.: Technical drawing of 4 bars together with 15 scintillator tiles by D. Pristauz-Telsnigg. The additional SiPMs can be seen together with their cable connectors on the front side, on the top left four lightguides can be seen in blue.

BGO Readout

The photo multiplier tubes previously used for the BGO do not provide readout in block transfer mode and therefore cannot be used in combination with the new DAQ setup. For that reason they will be replaced by SiPMs positioned on the outside of the vacuum window.

The CAEN V1190B which is at the moment used for the fibres will be then recording the signals on the BGO in 63 channels (one channel needs to be reserved for trigger recording).

Data Analysis

For the development of the new data acquisition system only the `analyser` programme was changed, which is only a pre-analysis of the binary data. In order to perform event identification and three dimensional particle tracking, the algorithm developped by B. Kolbinger [16] will need to be adjusted.

Appendix

List of Abbreviations

A

AMT ASACUSA Micromegas Tracker

APD avalanche photodiode

AD Antiproton Decelerator

ADC analogue to digital converter

ASACUSA Atomic Spectroscopy And Collisions Using Slow Antiprotons

BGO $Bi_4Ge_3O_{12}$

BLT block transfer

CERN Conseil Européen pour la Recherche Nucléaire

CLI command line interface

DAQ data acquisition

ECL emitter coupled logic

EFI external field ionizer

ELENA Extra Low Energy Antiprotons

FI field ionization

FIFO first in - first out

FPGA field programmable gate array

FWHM full width at half maximum

HFS high field seeking

IFES intelligend frontend electronics for SiPMs

LE leading edge

LFS low field seeking

LI Lorentz invariance

LS2 Long Shutdown 2

LVDS low voltage differential signal

Micromegas Micro-MEsh GAseous Structure

MIDAS Maximum Integrated Data Acquisition System

MRE multi-ring electrode

MUSASHI Monoenergetic Ultra-Slow Antiproton Source for High-precision Investigation

NIM nuclear instrumentation standard

ODB online database

PMT photo multiplier tube

PS proton synchrotron

PSI Paul Scherrer Institute

SiPM silicon photo multiplier

SM Standard Model of particle physics

SMI Stefan Meyer Institute

SME Standard Model Extension

TDC time-to-digital converter

TE trailing edge

ToF time-of-flight

ToT time-over-threshold

TRIUMF Tri University Meson Facility

VHDL Very High Speed Integrated Circuit Hardware Description Language

VME Versa Module Europa

Additional Tables and Figures

B

Tab. B.1.: Detector materials currently used in the detector.

Type	Description	Size	Quantity
EJ-200	scintillator, inner hodoscope bars	$450 \times 35 \times 5\,\mathrm{mm}^3$	32
EJ-200	scintillator, outer hodoscope bars	$300 \times 20 \times 5\,\mathrm{mm}^3$	32
BGO	scintillator, central calorimeter	90 mm diameter, 5 mm thickness	1
PM3350-TS	SiPM, hodoscope readout	$3 \times 3\,\mathrm{mm}^2$	256
BCF-12	scintillating fibres	$2 \times 2\,\mathrm{mm}^2$	656
PM3350-EB	SiPM, fibre readout	$3 \times 3\,\mathrm{mm}^2$	164

Tab. B.2.: Channel mapping of amplifier board channels and fibre detector channels. The boards are labelled by their IDs. Empty channels are denoted by '–', channels on the inner layer with 'i' and channels on the outer layer with 'o'. Table is from [39].

Board	Board Channels															
ID	0	1	2	3	4	5	6	7	8	9	10	11	12	13	14	15
10	–	99o	91o	83o	75o	67o	59o	51o	–	–	–	–	61i	53i	45i	37i
11	50o	97o	89o	81o	73o	65o	57o	49o	60i	52i	44i	36i	59i	51i	43i	35i
12	8i	16i	24i	32i	1i	9i	17i	25i	22o	30o	46o	7o	15o	23o	31o	39o
13	–	98o	90o	82o	74o	–	66o	58o	–	–	–	–	58i	50i	42i	34i
14	63o	55o	96o	88o	80o	72o	64o	56o	–	57i	49i	41i	33i	56i	48i	40i
15	38o	47o	8o	16o	24o	32o	40o	48o	1o	9o	17o	25o	33o	41o	2o	10o
16	2i	10i	18i	26i	3i	11i	19i	27i	18o	26o	34o	42o	3o	11o	27o	19o
17	44o	36o	28o	20o	12o	4o	43o	35o	28i	20i	12i	4i	29i	21i	13i	5i
18	–	100o	92o	84o	76o	68o	60o	52o	62i	54i	46i	38i	63i	55i	39i	47i
19	53o	54o	61o	62o	69o	70o	71o	77o	78o	79o	85o	86o	87o	93o	94o	95o
20	6i	14i	22i	30i	7i	15i	23i	31i	5o	13o	21o	29o	37o	45o	6o	14o

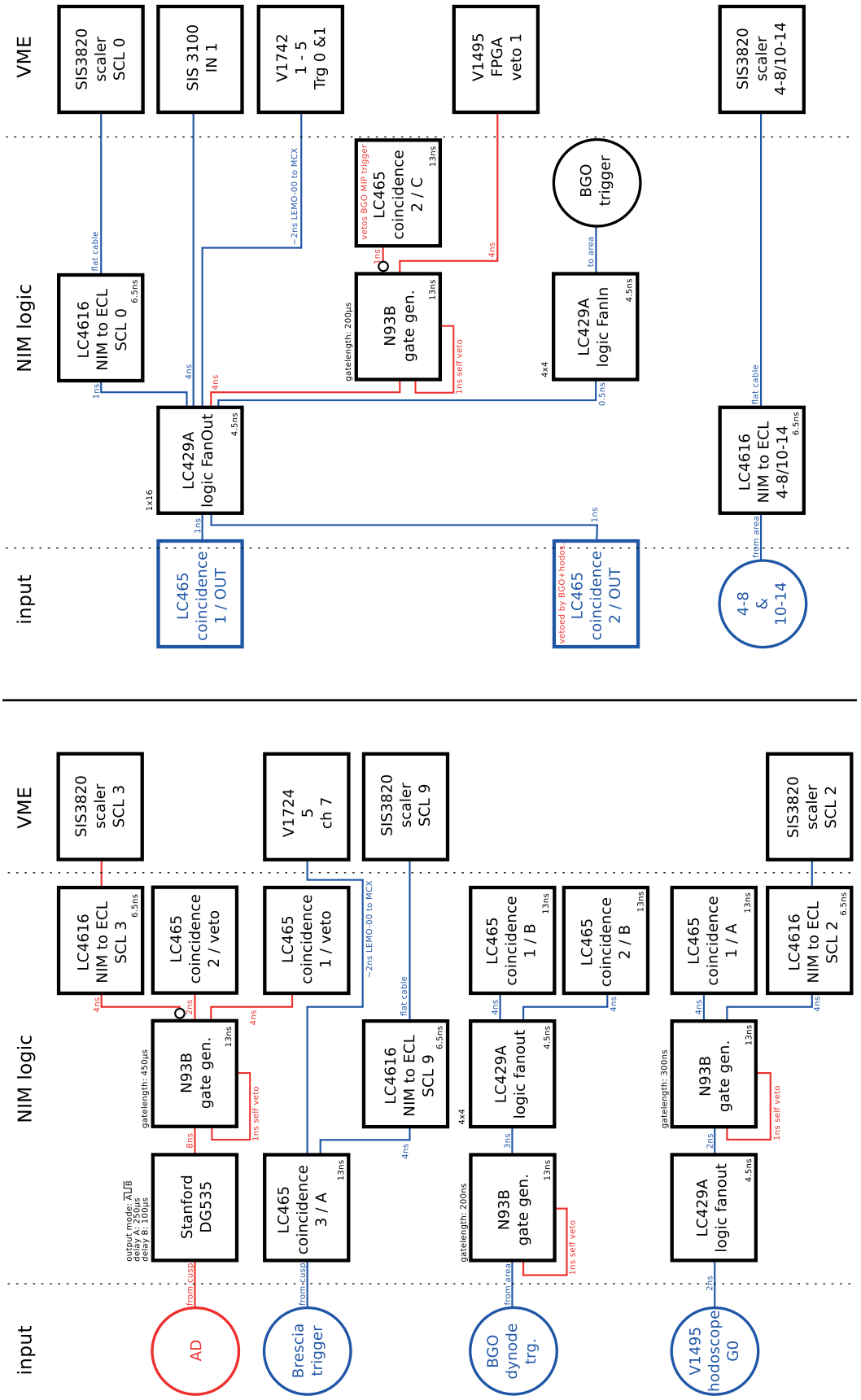

Fig. B.1.: Trigger flow diagrams before a coincidence unit (left part) and after (right part) [37]. Trigger signals are blue, veto signals are red. The circled signals are coming from or going to the experimental area, NIM modules are drawn as rectangles. The labels show the delays.

Listing B.1: Definition of the Trigger Equipment in the new frontend.

```
EQUIPMENT equipment[] = {

  {"Trigger",               /* equipment name */
   {1, 0,                   /* event ID, trigger mask */
    "SYSTEM",               /* event buffer */
    EQ_POLLED,              /* equipment type */
    LAM_SOURCE(0, 0xFFFFFFFF),/* event source */
    "MIDAS",                /* format */
    TRUE,                   /* enabled */
    RO_RUNNING,             /* read only when running */

    10,                     /* poll for 10ms */
    0,                      /* stop run after this event limit */
    0,                      /* number of sub events */
    0,                      /* don't log history */
    "", "", "",}
   ,
   read_tdc_event,          /* readout routine */
   NULL, NULL,
   NULL,                    /* bank list */
  }
  ,

  {""}
}
```

Listing B.2: Readout routine for the new frontend

```
INT read_tdc_event(char *pevent, INT off)
{
    WORD *pdata;
    \\ Start SIS Veto OUT1 and OUT2:
    s3100_control_write(vme->handle,0x080, 0x01000000);
    s3100_control_write(vme->handle,0x080, 0x02000000);

    bk_init32(pevent);

    // create bank for run number:
    DWORD *run;
    bk_create(pevent, "RUNN", TID_DWORD, &run);
    *run++ = cuspRunNumber;
    bk_close(pevent,run);

    // create bank for midas timestamp in milliseconds:
    DOUBLE *pdata2;
    bk_create(pevent, "MILT", TID_DOUBLE, &pdata2);
    *pdata2++ = MidasMilliTimeStart - ss_millitime();
    bk_close(pevent,pdata2);

    cm_msg(MINFO, "vmefrontend","start of TDC readout");

    std::chrono::time_point<std::chrono::high_resolution_clock>
    t_start = std::chrono::high_resolution_clock::now();

    // calls v1190.cc, where TDC banks are filled
    for(int i=0; i<numOfV1190; i++){
        tdcs[i]->read(pevent);
        cm_msg(MINFO, "vmefrontend","TDC%i read", i);
    }

    std::chrono::time_point<std::chrono::high_resolution_clock> t_end =
    std::chrono::high_resolution_clock::now();
    std::chrono::duration<float> diff = t_end-t_start;

    cm_msg(MINFO, "vmefrontend","TDC read time %f sec", diff.count() );

    // Stop SIS Veto OUT1 and OUT2:
    s3100_control_write(vme->handle,0x080, 0x00010000);
    s3100_control_write(vme->handle,0x080, 0x00020000);

    return bk_size(pevent);
}
```

Tab. B.3.: Channel mapping for the TDCs used by the `analyser` . Channels with 999 mean that they are not used. Positive channels are from outer bars/fibres, negative channels are inner bars/fibres. The channels between |200| and |300| are for downstream SiPMs, the ones above |300| are for the upstream SiPMs. The lower two digits are equal to the bar number in the hodoscope.

Board ID	Board channels 1 to 16															
13	999	98	90	82	74	999	66	58	999	999	999	999	-58	-50	-42	-34
12	-8	-16	-24	-32	-1	-9	-17	-25	22	30	46	7	15	23	31	39
11	50	97	89	81	73	65	57	49	-60	-52	-44	-36	-59	-51	-43	-35
10	500	99	91	83	75	67	59	51	999	999	999	999	-61	-53	-45	-37
14	63	55	96	88	80	72	64	56	999	-57	-49	-41	-33	-56	-48	-40
20	-6	-14	-22	-30	-7	-15	-23	-31	5	13	21	29	37	45	6	14
19	53	54	61	62	69	70	71	77	78	79	85	86	87	93	94	95
18	999	100	92	84	76	68	60	52	-62	-54	-46	-38	-63	-55	-39	-47
17	44	36	28	20	12	4	43	35	-28	-20	-12	-4	-29	-21	-13	-5
16	-2	-10	-18	-26	-3	-11	-19	-27	18	26	34	42	3	11	27	19
15	38	47	8	16	24	32	40	48	1	9	17	25	33	41	2	10
	501	502	503	504	505	506	507	508	509	510	511	512	513	514	515	516
1	204	205	206	207	208	209	210	211	-204	-205	-206	-207	-208	-209	-210	-211
2	212	213	214	215	216	217	218	219	-212	-213	-214	-215	-216	-217	-218	-219
3	220	221	222	223	224	225	226	227	-220	-221	-222	-223	-224	-225	-226	-227
4	228	229	230	231	200	201	202	203	-228	-229	-230	-231	-200	-201	-202	-203
5	-319	-318	-317	-316	-315	-314	-313	-312	319	318	317	316	315	314	313	312
6	-311	-310	-309	-308	-307	-306	-305	-304	311	310	309	308	307	306	305	304
7	-327	-326	-325	-324	-323	-322	-321	-320	327	326	325	324	323	322	321	320
8	-303	-302	-301	-300	-331	-330	-329	-328	303	302	301	300	331	330	329	328

Listing B.3: The function `fillData` used in the `analyser` . For simplicity only the filling of the inner hodoscope leading edges is shown, filling the other channels works similarly.

```
bool fillData(std::vector<int> chanData, hodoscopeEvent *data){

 printf("--------- Readout finished ----------\n");

 int nr_ch = 15000;

  if (chanData.size() > 0)
  {
    for(unsigned int j=3; j <= chanData.size(); j+=4)
    {
    int32_t ch = chanData[j-3];      // Assigned channel (Tab. B.2)
    int32_t rawch = chanData[j-2];  // TDC channel

       if (chanData[j-1] == 0) {     // Leading Edges

         if (ch<0) {         // Inner Hodoscope

            if (ch <= -200 && ch >-300){
                ch = (ch+200)*(-1);
                    if (data->HodoTdcLEInnerDownstream[ch] > nr_ch){
                        data->HodoTdcLEInnerDownstream[ch] = 0;
                    }
                    if (data->HodoTdcLEInnerDownstream[ch] < 0){
                        data->HodoTdcLEInnerDownstream[ch] = 0;
                    }
                    if (data->HodoTdcLEInnerDownstream[ch] != 0 &&
                    chanData[j] > data->HodoTdcLEInnerDownstream[ch] )
                        continue; // only first hits are used

                    data->HodoTdcLEInnerDownstream[ch] = chanData[j];
            printf("#### Wrote %i into HodoTdcLEInnerDownstream[%i]\n",
            chanData[j], ch);

            } else if (ch <= -300 && ch>-400){
                ch = (ch+300)*(-1);
                    if (data->HodoTdcLEInnerUpstream[ch] > nr_ch){
                        data->HodoTdcLEInnerUpstream[ch] = 0;
                    }
                    if (data->HodoTdcLEInnerUpstream[ch] < 0){
                        data->HodoTdcLEInnerUpstream[ch] = 0;
                    }
                    if (data->HodoTdcLEInnerUpstream[ch] != 0 &&
                    chanData[j] > data->HodoTdcLEInnerUpstream[ch])
                        continue;
                    data->HodoTdcLEInnerUpstream[ch] = chanData[j];
            printf("#### Wrote %i into HodoTdcLEInnerUpstream[%i]\n",
            chanData[j], ch);

            } else {
```

```
                ch = ch*(-1);
                    if (data->TdcLEInner[ch] > nr_ch){
                        data->TdcLEInner[ch] = 0;
                    }
                    if (data->TdcLEInner[ch] < 0){
                        data->TdcLEInner[ch] = 0;
                    }
                    if (data->TdcLEInner[ch] != 0 &&
                    chanData[j] > data->TdcLEInner[ch])
                        continue;
                    data->TdcLEInner[ch] = chanData[j];
            printf("#### Wrote %i into TdcLEInner[%i]\n",
            chanData[j],ch);

            }

        } else {   // Outer Hodoscope

            // ... readout of outer hodoscope leading edges left out

        }


      } else if (chanData[j-1] == 1) {      // Trailing Edges

        // ... readout of trailing edges left out

      }

        ////////////////////////////////////////////////////////////
   }

   printf("----------- Write finished ------------\n");
  }

    return true;

}
```

C

List of Figures

List of Tables

D

Bibliography

E

[1] E. Noether. Invariante Variationsprobleme. *Nachrichten von der Gesellschaft der Wissenschaften zu Göttingen, Mathematisch-Physikalische Klasse*, 1918:235–257, 1918.

[2] C. S. Wu, E. Ambler, R. W. Hayward, et al. Experimental test of parity conservation in beta decay. *Physical Review*, 105(4):1413–1415, 1957. doi:10.1103/PhysRev.105.1413.

[3] J. H. Christenson, J. W. Cronin, V. L. Fitch, and R. Turlay. Evidence of the 2π decay of the K_2^0 meson. *Physical Review Letters*, 13(4), 1964.

[4] M. E. Peskin, D. V. Schroeder, and E. Martinec. *An Introduction to Quantum Field Theory*, volume 49. 1996. ISBN 9780201503975. doi:10.1063/1.2807734, `http://physicstoday.scitation.org/doi/10.1063/1.2807734`.

[5] D. Sakharov. Violation of CP invariance, C asymmetry, and baryon asymmetry of the universe. *Soviet Physics - Uspekhi*, 34(5):392–393, 1991. doi:10.1070/PU1991v034n05ABEH002497.

[6] O. Bertolami, D. Colladay, V. A. Kostelecký, and R. Potting. CPT violation and baryogenesis. *Physics Letters, Section B: Nuclear, Elementary Particle and High-Energy Physics*, 395(3-4):178–183, 1997. doi:10.1016/S0370-2693(97)00062-2.

[7] H. Hellwig, D. W. Allan, D. J. Glaze, et al. Measurement of the Unperturbed Hydrogen Hyperfine Transition Frequency. *IEEE Transactions on Instrumentation and Measurement*, 19(4):200–209, 1970. doi:10.1109/TIM.1970.4313902.

[8] N. F. Ramsey. Experiments with Separated Oscillatory Fields and Hydrogen Masers (Nobel Lecture). *Reviews of Modern Physics*, 62(3):541–552, 1990. doi:10.1002/anie.199007251.

[9] M. Diermaier, C. B. Jepsen, B. Kolbinger, et al. In-beam measurement of the hydrogen hyperfine splitting and prospects for antihydrogen spectroscopy. *Nature Communications 2017 8:1*, 8(1):1–9, 2017. doi:10.1038/ncomms15749.

[10] P. Kusch. Redetermination of the Hyperfine Splittings of Hydrogen and Deuterium in the Ground State. *Physical Review*, 100(4):1188–1190, 1955. doi:10.1103/PhysRev.100.1188.

[11] G. Breit and I. I. Rabi. Measurement of nuclear spin. *Physical Review*, 38(11): 2082–2083, 1931. doi:10.1103/PhysRev.38.2082.2.

[12] I. I. Rabi. On the Process of Space Quantization. *Physical Review*, 49(4):324–328, 1936. doi:10.1103/PhysRev.49.324.

[13] R. Bluhm, V. A. Kostelecký, and N. Russell. CPT and lorentz tests in hydrogen and antihydrogen. *Physical Review Letters*, 82(11):2254–2257, 1999. doi:10.1103/PhysRevLett.82.2254.

[14] V. A. Kostelecký and N. Russell. Data tables for Lorentz and CPT violation. *Reviews of Modern Physics*, 83(1):11–31, 2011. doi:10.1103/RevModPhys.83.11.

[15] V. A. Kostelecký and A. J. Vargas. Lorentz and CPT tests with hydrogen, antihydrogen, and related systems. *Physical Review D - Particles, Fields, Gravitation and Cosmology*, 92, 2015. doi:10.1103/PhysRevD.92.056002.

[16] B. Kolbinger. *Machine Learning for Antihydrogen Detection in ASACUSA*. PhD thesis, University of Vienna, 2019.

[17] M. Hori, K. Yamashita, R. S. Hayano, and T. Yamazaki. Analog Cherenkov detectors used in laser spectroscopy experiments on antiprotonic helium. *Nuclear Instruments and Methods in Physics Research, Section A: Accelerators, Spectrometers, Detectors and Associated Equipment*, 496(1):102–122, 2003. doi:10.1016/S0168-9002(02)01618-2.

[18] W. R. Leo. *Techniques for Nuclear and Particle Physics Experiments*. Springer Berlin Heidelberg, Berlin, Heidelberg, 2., rev. e edition, 1994. ISBN 978-3-540-57280-0. doi:10.1007/978-3-642-57920-2, http://link.springer.com/10.1007/978-3-642-57920-2.

[19] ELJEN. GENERAL PURPOSE EJ-200, EJ-204, EJ-208, EJ-212, 2021, https://eljentechnology.com/products/plastic-scintillators/ej-200-ej-204-ej-208-ej-212 (accessed: 2022-10-01).

[20] Saint-Gobain. BGO Scintillation Material, 2021, https://www.crystals.saint-gobain.com/radiation-detection-scintillators/crystal-scintillators/bgo-bismuth-germanate# (accessed: 2022-10-01).

[21] KETEK. SiPM Working Principle, https://www.ketek.net/sipm/technology/working-principle/ (accessed: 2021-10-07).

[22] KETEK. Product Data Sheet PM3325-EB / PM3350-EB, 2017, https://www.ketek.net/wp-content/uploads/2017/01/KETEK-PM3325-EB-PM3350-EB-Datasheet.pdf (accessed: 2022-10-01).

[23] S. Baird, D. Berlin, J. Boillot, et al. Design study of the antiproton decelerator: AD. Technical Report November 1996, CERN, Geneva, 1996, http://cds.cern.ch/record/317704.

[24] M. Hori and J. Walz. Physics at CERN's antiproton decelerator. *Progress in Particle and Nuclear Physics*, 72:206–253, 2013. doi:10.1016/j.ppnp.2013.02.004.

[25] W. Oelert. The ELENA project at CERN. *Acta Physica Polonica B*, 46(1), 2015. doi:10.5506/APhysPolB.46.181.

[26] W. Bartmann, P. Belochitskii, H. Breuker, et al. The ELENA facility. *Philosophical Transactions of the Royal Society A: Mathematical, Physical and Engineering Sciences*, 376(2116), 2018. doi:10.1098/RSTA.2017.0266.

[27] N. Kuroda, H. A. Torii, Y. Nagata, et al. Development of a monoenergetic ultraslow antiproton beam source for high-precision investigation. *Physical Review Special Topics - Accelerators and Beams*, 15(2):024702, 2012. doi:10.1103/PhysRevSTAB.15.024702.

[28] H. Imao, K. Michishio, Y. Kanai, et al. Positron accumulation and manipulation for antihydrogen synthesis. *Journal of Physics: Conference Series*, 225, 2010. doi:10.1088/1742-6596/225/1/012018.

[29] Y. Nagata, N. Kuroda, P. Dupre, et al. Progress of Antihydrogen Beam Production Using a Double Cusp Trap. In *Proceedings of the 12th International Conference on Low Energy Antiproton Physics (LEAP2016)*. Journal of the Physical Society of Japan, 2017. ISBN 4-89027-125-2. doi:10.7566/JPSCP.18.011007, `https://doi.org/10.7566/JPSCP.18.011007http://journals.jps.jp/doi/10.7566/JPSCP.18.011007`.

[30] M. Tajima, N. Kuroda, C. Amsler, et al. Antiproton beams with low energy spread for antihydrogen production. *Journal of Instrumentation*, 14(05):P05009, 2019. doi:10.1088/1748-0221/14/05/P05009.

[31] B. Radics, Y. Nagata, Y. Yamazaki, et al. The ASACUSA Micromegas Tracker: A cylindrical, bulk Micromegas detector for antimatter research. *Review of Scientific Instruments*, 86(8):083304, 2015. doi:10.1063/1.4927685.

[32] N. Kuroda, S. Ulmer, D. J. Murtagh, et al. A source of antihydrogen for in-flight hyperfine spectroscopy. *Nature Communications*, 5, 2014. doi:10.1038/NCOMMS4089.

[33] B. Radics, D. J. Murtagh, Y. Yamazaki, and F. Robicheaux. Scaling behavior of the ground-state antihydrogen yield as a function of positron density and temperature from classical-trajectory Monte Carlo simulations. *Physical Review A*, 90(3):032704, 2014. doi:10.1103/PhysRevA.90.032704.

[34] N. Kuroda, S. Ulmer, D. J. Murtagh, et al. Towards a spin polarized antihydrogen beam. *Hyperfine Interactions*, 228(1-3):67–76, 2014. doi:10.1007/s10751-014-1016-9.

[35] Y. Nagata, N. Kuroda, M. Ohtsuka, et al. Direct detection of antihydrogen atoms using a BGO crystal. 2016. doi:10.1016/j.nima.2016.10.019.

[36] Stefan-Meyer-Institute. Detector Development, `https://www.oeaw.ac.at/smi/research/advanced-instrumentation/detector-development` (accessed: 2022-02-04).

[37] C. Sauerzopf. *The ASACUSA Antihydrogen Detector: Development and Data Analysis*. PhD thesis, Technical University of Vienna, 2016.

[38] C. Sauerzopf, L. Gruber, K. Suzuki, et al. Intelligent Front-end Electronics for Silicon photodetectors (IFES). *Nuclear Instruments and Methods in Physics Research Section A: Accelerators, Spectrometers, Detectors and Associated Equipment*, 819: 163–166, 2016. doi:10.1016/j.nima.2016.02.098.

[39] M. Fleck. *The Development and Implementation of a Fibre Detector and Advanced Data Acquisition for the ASACUSA Antihydrogen Detector*. PhD thesis, Technical University of Vienna, 2018.

[40] CAEN S.p.A. V1190A-2eSST 128 Channel Multihit TDC (100/200/800 ps), , `https://www.caen.it/products/v1190a-2esst/` (accessed: 2021-11-04).

[41] CAEN S.p.A. V1190B-2eSST 64 Channel Multihit TDC (100/200/800 ps), , `https://www.caen.it/products/v1190b-2esst/` (accessed: 2021-11-04).

[42] R. Brun and F. Rademakers. ROOT - An Object Oriented Data Analysis Framework. *Nuclear Instruments and Methods in Physics and Research Section A*, 389 (Proceedings AIHENP'96 Workshop, Lausanne, Sep. 1996):81–86, 1997.

[43] F. Rademakers, P. Canal, A. Naumann, et al. root-project/root: v6.20/06. 2020. doi:10.5281/ZENODO.3895852.

[44] CAEN S.p.A. V2495 Programmable Logic Unit PLUS, , `https://www.caen.it/products/v2495/` (accessed: 2021-11-04).

[45] CAEN S.p.A. SCI-Compiler - User Firmware Generator and Compiler for CAEN Programmable Boards, , `https://www.caen.it/products/sci-compiler/` (accessed: 2021-11-04).

[46] PSI and TRIUMF. MIDAS Wiki, `https://midas.triumf.ca/MidasWiki/index.php?title=Main_Page&oldid=2982` (accessed: 2021-12-09).

[47] C. Sauerzopf. waveformlibrary v1.0.0, 2015. doi:10.5281/zenodo.35341.

[48] CAEN S.p.A. Mod. V1190-VX1190 A/B, 128/64 Ch Multihit TDC. *Technical Information Manual*, 2016.

[49] Thorlabs. Round Continuouslly Variable Metallic Neutral Density Filters, https://www.thorlabs.com/newgrouppage9.cfm?objectgroup_id=1393&pn=NDC-50C-4M#1390 (accessed: 2020-11-28).

[50] B. Kolbinger, C. Amsler, S. A. Cuendis, et al. Measurement of the principal quantum number distribution in a beam of antihydrogen atoms. *European Physical Journal D*, 75(3), 2021. doi:10.1140/epjd/s10053-021-00101-y.